Continuous endosomes form functional subdomains and orchestrate rapid membrane trafficking in trypanosomes

Authors:

Fabian Link[1], Alyssa Borges[1], Oliver Karo[1], Marvin Jungblut[2], Thomas Müller[1], Elisabeth Meyer-Natus[1], Timothy Krüger[1], Stefan Sachs[2], Nicola G. Jones[1], Mary Morphew[3], Markus Sauer[2], Christian Stigloher[4], J. Richard McIntosh[3], Markus Engstler[1]

Affiliations:

[1]Department of Cell & Developmental Biology, Biocentre, University of Würzburg, 97074 Würzburg, Germany

[2]Department of Biotechnology & Biophysics, Biocentre, University of Würzburg, 97074 Würzburg, Germany

[3]Molecular, Cellular & Developmental Biology, University of Boulder, Colorado, USA

[4] Imaging Core Facility, Biocentre, University of Würzburg, 97074 Würzburg, Germany

Corresponding authors: Markus Engstler (markus.engstler@uni-wuerzburg.de)

Keywords:

Membrane recycling, African trypanosomes, Endocytosis, Rab proteins, Tokuyasu, Tomography

Abstract

Endocytosis is a common process observed in all eukaryotic cells, although its complexity varies among different organisms. In *Trypanosoma brucei*, the endocytic machinery is under special selective pressure because rapid membrane recycling is essential for immune escape. This unicellular parasite effectively removes host antibodies from its cell surface through hydrodynamic drag and fast endocytic internalization. The entire process of membrane recycling occurs exclusively through the flagellar pocket, an extracellular organelle situated at the posterior pole of the spindle-shaped cell. The high-speed dynamics of membrane flux in trypanosomes do not seem compatible with the conventional concept of distinct compartments for early, late and recycling endosomes. To investigate the underlying structural basis for the remarkably efficient membrane traffic in trypanosomes, we employed advanced techniques in light and electron microscopy to examine the three-dimensional architecture of the endosomal system. Our findings reveal that the endosomal system in trypanosomes exhibits a remarkably intricate structure. Instead of being compartmentalized, it constitutes a continuous membrane system, with specific functions of the endosome segregated into membrane subdomains enriched with classical markers for early, late, and recycling endosomes. These membrane subdomains can partly overlap or are interspersed with areas that are negative for endosomal markers. This continuous endosome allows fast membrane flux by facilitated diffusion that is not slowed by multiple fission and fusion events. Our study further suggests that in trypanosomes, the endosome has taken over the role of the trans-Golgi network as the master regulator of membrane trafficking.

Introduction

Endocytosis research has traditionally focused on a limited number of organisms, primarily opisthokonts (including yeast and humans). Recently, using the extensive genetic and cell biological resources now available for studying numerous other organisms, studies on protists such as *Dictyostelium*, *Giardia*, *Toxoplasma* or trypanosomes have revealed remarkable deviations from the hitherto existing understanding of the processes of endo- and exocytosis described in textbooks (reviewed in Benchimol and de Souza, 2022; Link et al., 2021; McGovern et al., 2021; Vines and King, 2019). Looking at the distinct evolutionary solutions for endosomal recycling across different branches of the eukaryotes, these protists, and especially the parasites among them, are of particular interest.

Throughout their life cycle, parasites often encounter a series of inherently hostile environments. The arms race between the parasite and its host has resulted in coevolutionary processes characterized by intense reciprocal selective pressures. Although parasite and host use similar basic cell biological pathways, parasites have often optimised these, either to achieve maximum efficiency or to establish additional functions. In this regard, the endocytosis and membrane recycling mechanisms observed in African trypanosomes serve as a remarkable illustration of the exceptional functional adaptations exhibited by parasites in response to their specific host environments.

Trypanosoma brucei is a representative of the group Discoba, which diverged before the appearance of opisthokonts (Burki et al., 2020; Strassert et al., 2021). *T. brucei* is an exclusively extracellular parasite, that resists the harsh conditions within the bloodstream, interstitial fluids and lymph and thus thrives in the body fluids of its vertebrate host's. Additionally, the cells have adapted to entirely distinct, yet equally challenging environments within the transmitting insect vector, *Glossina* (tsetse fly). Within the midgut of the fly, the trypanosomes proliferate to very high densities and, following a several week long journey, attach to the insect salivary glands before being injected back into the host skin during the bloodmeal of the tsetse (Rose et al., 2020).

The extracellular lifestyle of *T. brucei* renders the parasite vulnerable to constant attacks by the host's immune system. In response, these parasites have evolved a protective surface coat covering the entire plasma membrane (Cross, 1975). This coat comprises a single type of variant surface glycoprotein (VSG) and forms the basis of antigenic variation (Mugnier et al., 2016). *T. brucei* possesses hundreds of VSG genes that encode structurally similar yet antigenically

distinct proteins (Taylor and Rudenko, 2006). However, only one VSG gene is expressed at a time, originating from a polycistronic expression site located at the telomere of the chromosomes (Becker et al., 2004; Chaves et al., 1999). The stochastic switching to the expression of a new VSG guarantees that the parasites remain ahead of the host immune response.

Antigenic variation is not the sole defense strategy employed against the host´s immune reaction. During immune attack, parasites actively remove anti-VSG antibodies from their cell surface. This process of antibody clearance is driven by hydrodynamic drag forces resulting from the continuous directional movement of trypanosomes (Engstler et al., 2007). The VSG-antibody complexes on the cell surface are dragged against the swimming direction of the parasite and accumulate at the posterior pole of the cell. This region harbours an invagination in the plasma membrane known as the flagellar pocket (FP) (Gull, 2003; Overath et al., 1997). The FP, which marks the origin of the single attached flagellum, is the exclusive site for endo- and exocytosis in trypanosomes (Gull, 2003; Overath et al., 1997). Consequently, the accumulation of VSG-antibody complexes occurs precisely in the area of bulk membrane uptake. For the process of antibody clearance to function efficiently, several conditions must be met. The VSG coat must be densely packed to prevent immune recognition of non-variant surface proteins, VSG must be highly mobile to allow the drag forces to take effect, and endocytosis must be sufficiently rapid to internalize the VSG-antibody complexes effectively. Furthermore, endosomal sorting and membrane recycling must keep pace with the bulk membrane uptake to maintain membrane balance. In fact, the VSG coat is as densely packed as physically possible (Hartel et al., 2016) and VSG molecules possess a flexible C-terminal domain attached via a GPI-anchor to the outer leaflet of the plasma membrane (reviewed in Borges et al., 2021). This lipid anchoring enables the highly dynamic behaviour of the VSG coat (Bartossek et al., 2017), further facilitated by N-glycans that insulate VSG molecules, thereby minimizing protein-protein interactions (Hartel et al., 2016). VSG molecules exhibit diffusion on the plasma membrane with coefficients that enable fast randomization (Hartel et al., 2016; Schwebs et al., 2022). This rapid VSG diffusion is precisely balanced with membrane recycling kinetics, with one surface equivalent being internalized and recycled within 12 minutes (Engstler et al., 2004). This exceptionally fast endocytosis is crucial for antibody clearance.

To summarize, *T. brucei* has evolved a series of interconnected cell biological adaptations in order to evade the immune system, ranging from a highly polarized cell structure and constant

directional motion to the generation of a variable, densely packed yet highly mobile cell surface coat, as well as an unusually rapid endocytosis machinery. The strong selective pressure acting on trypanosomes has led to the integration and coordination of seemingly unrelated features, such as cell motility, surface protein dynamics, clathrin-mediated endocytosis, protein sorting, and membrane recycling. This illustrates the extraordinary cell biology of parasitic protozoa, which offers functional linkages beyond that of yeast or mammalian cells.

In this study, we aimed to solve a problem related to the rapid membrane recycling observed in trypanosomes. Specifically, we investigated the structural basis underlying the rapid kinetics of membrane flow and cargo sorting in these organisms. Trypanosomes internalize approximately 150 μm^2 of membrane in about 10 minutes, exclusively via clathrin-mediated endocytosis and solely through the flagellar pocket (Engstler et al., 2004; Grünfelder et al., 2002; Grünfelder et al., 2003). Within the same timeframe, the VSG coat must also be efficiently recycled back to the cell surface, again via the flagellar pocket. This turbulent traffic at the flagellar pocket must be reflected in the membrane flux through the endosomal compartments.

In *T. brucei*, the process of endocytosis (reviewed in Link et al., 2021) begins with the formation of clathrin-coated vesicles (CCVs) at the flagellar pocket membrane (Allen et al., 2003; Morgan et al., 2001). Subsequently, both membrane-bound VSG and fluid-phase cargo pass through early endosomes (EE) (Engstler et al., 2004; Grünfelder et al., 2003). From this compartment, both either move directly to the recycling endosomes (RE) and return to the cell surface or first pass from the EE to the late endosomes (LE) before returning to the surface via the RE (Engstler et al., 2004). Alternatively, fluid-phase cargo can be directed from LEs to the lysosome for degradation (Engstler et al., 2004). The endosomal subpopulations in *T. brucei* are characterized by the canonical marker proteins, including TbRab5A (EE), TbRab7 (LE), and TbRab11 (RE), as well as by their morphology (Engstler et al., 2004; Grünfelder et al., 2003; Overath and Engstler, 2004). TbRab5A-positive endosomal structures have been described as circular or elongated cisternae, while TbRab7-positive structures exhibit an irregular shape (Engstler et al., 2004; Grünfelder et al., 2003; Overath and Engstler, 2004). Additionally, TbRab11-positive structures are characterized as either elongated cisternae or disk-shaped exocytic carriers (Grünfelder et al., 2003).

A thorough examination of the kinetics of endosomal recycling has validated the rapid passage through various endosomal compartments (Engstler et al., 2004; Grünfelder et al., 2003). However, these analyses have not addressed how the kinetics can be reconciled with the

occurrence of multiple fission and fusion events that are thought to accompany endosomal transport through these compartments.

Here, we have employed a comprehensive set of techniques to scrutinize the ultrastructure of specific endosomal subdomains in *T. brucei*. In addition to utilizing electron tomography, super-resolution fluorescence microscopy and colocalization analysis, we have introduced Tokuyasu sectioning for 3D immuno-electron microscopy. These tools allowed us to elucidate the structural basis for the remarkable speed of endosomal recycling in trypanosomes.

Results

The endosomal apparatus of *T. brucei* is a large intricate structure

In order to generate an overview of the endosomal ultrastructure in bloodstream form (BSF) trypanosomes, we performed electron tomography after fluid phase cargo uptake assays with horseradish peroxidase (HRP) and ferritin (Figure 1). Fluid phase cargo was selected as it ensures a comprehensive labelling of all endosomal compartments (Engstler et al., 2004). Following HRP/ferritin endocytosis, the cells were fixed and embedded in Epon resin. To visualize HRP, photooxidation with 3,3'-diaminobenzidine (DAB) was employed before acquiring tomographic data (Figure 1 A, B, and D). Analysis of the reconstructed electron tomograms of various BSF cells revealed a morphologically intricate system of endosomes comprised of interconnected and fenestrated membrane networks. The main endosome, spanning the posterior region of the cell from the vicinity of the flagellar pocket (FP) to the Golgi apparatus, exhibited elongated (Figure 1 A and B) and circular membrane sheets (Figure 1 C and D), encompassing a volume with a diameter of approximately 2 µm and a length of 4 µm. The localization of endosomes was strictly confined to the posterior cytoplasm. Their precise positioning, however, appeared to be flexible, indicating a lack of direct and rigid connection with the microtubule cytoskeleton. This observation is not surprising, as microtubules form the dense subpellicular cytoskeleton in trypanosomes but are not detectable in the cytoplasm. Moreover, the cytoplasm is constantly agitated by the beat of the attached single flagellum. The electron tomograms further suggest that the large size of the endosomes may render them unable to pass through the space between the nucleus and pellicular microtubules. Another notable finding was the proximity of endosomes to the Golgi apparatus (Figure 1 A and B), suggesting a potential involvement of the endosomal system in post-Golgi transport. In summary, electron tomography analysis of cargo uptake assays provides evidence that the endosomal system in BSF cells is a complex, flexible, and largely continuous membrane network.

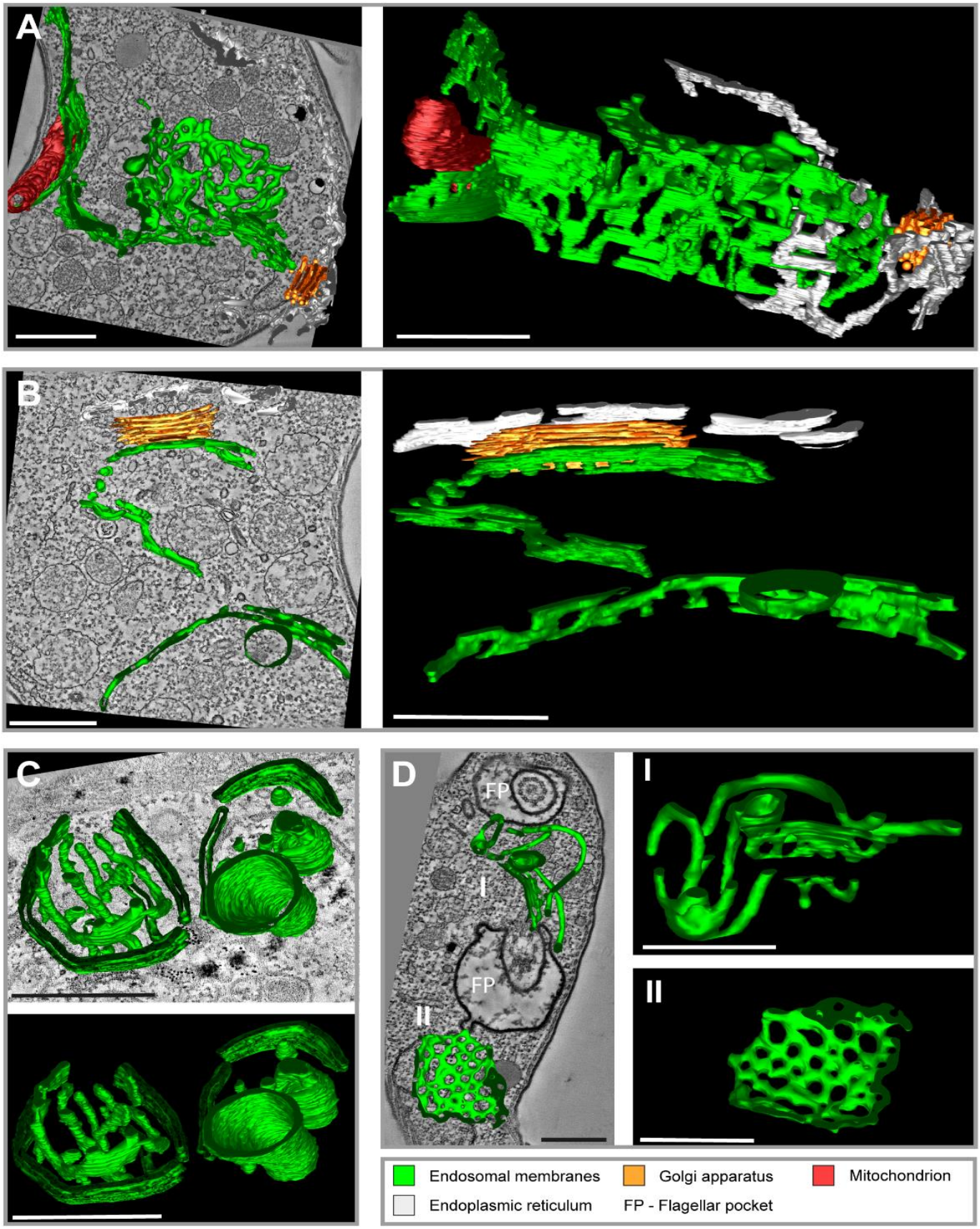
A
B
C
D
FP
I
FP
II
I
II
Endosomal membranes
Golgi apparatus
Mitochondrion
Endoplasmic reticulum
FP - Flagellar pocket

218

219

Figure 1. Tomographic reconstructions of the endosomal apparatus of *T. brucei* after cargo uptake reveals a large and mostly continuous membrane system. (A) Elongated and highly fenestrated endosomal sheets and palisades. **(B)** Elongated and slightly fenestrated endosomes. **(C)** Large circular endosomal cisternae. **(D)** Two different substructures are displayed: one contains tubular palisades (I) while the other one is a heavily fenestrated sheet (II). HRP endocytosis and DAB photooxidation were performed prior to tomogram acquisition (A, B and D). Ferritin endocytosis was performed prior to tomogram acquisition (C). All sections are 250 nm thick. The reconstructions (A) and (D) are based on three and two sections, respectively. The reconstructions (C) and (D) are based on one section each. The section and corresponding tomogram (C) originate from the same sample block as the image in Figure 4 I from Engstler et al. (2004). Endosomal membranes are shown in green. The endoplasmic reticulum is visualised in white colour. The Golgi apparatus is labelled in orange and the mitochondrion is shown in red. Abbreviation: flagellar pocket (FP). Scale bars: 500 nm. Movies corresponding to panel A-D can be found here: A) z-stack, 3D model; B) z-stack, 3D model; C) z-stack, 3D model; D) z-stack, 3D model.

Super-resolution microscopy reveals the endosomal apparatus as a largely continuous structure

To be able to do specific labelling of the endosomal compartment, we first tested the potential of various super-resolution light microscopy techniques to resolve and corroborate the structure of the entire endosomal compartment (Figure 2). To allow the identification of endosomes, we utilized the marker protein EP1 that had previously been demonstrated to label the entire endosome and flagellar pocket of bloodstream form trypanosomes (Engstler and Boshart, 2004). EP1, a cell surface protein found in insect stage trypanosomes, is mostly excluded from the VSG coat of bloodstream form (BSF) trypanosomes.

To utilize EP1 as an endosomal membrane marker in *direct* stochastic optical reconstruction microscopy (*d*STORM) (Heilemann et al., 2008), an EP1::HaloTag expressing cell line was generated (Figure S1). The transgenic parasites were then labelled with a HaloTag ligand conjugated to Alexa Fluor™ 647 (custom conjugated, see Methods), and imaged in 100 mM MEA photo-switching buffer (Figure 2 A).

As expected, the EP1::HaloTag signal was localized in the posterior region of the cell, between the nucleus and kinetoplast (Figure 2 A, I – II). Although the entire endosomal compartment seemed to be labelled and gave the appearance of a largely connected system (Figure 2 A, III – IV), the labelling density was not consistently strong, resulting in occasionally thin membrane bridges (Figure 2 A, upper row, image IV, indicated by an arrow). In addition, the 3D volume of the labelled region was too large (approx. 4 x 4 x 5 µm) to be completely captured by single-molecule localization microscopy. On top of that, not all cells exhibited an EP1::Halo signal, indicating heterogeneous gene expression within the population (Figure 2 A, lower row, lower cell).

To overcome the non-uniform labelling density based on an endogenous marker protein and to be able to capture the entire 3D volume of the parasite, a combination of dextran uptake assays and expansion microscopy (Chen et al., 2015) was performed to visualize the endosomes. The fluorescently labelled dextran was observed in the posterior region between the nucleus and kinetoplast in all cells (Figure 2 B). The expanded and unexpanded cells revealed elongated cable-like structures representing the endosomes, spanning from the flagellar pocket to the vicinity of the nucleus. The expansion process improved the resolution of the structure, allowing for the visualization of potential circular cisternae (Figure 2 B, middle row, image III, arrow). While the flagellar pocket labelling was visible in nearly all unexpanded cells, not all

expanded cells exhibited a corresponding signal (Figure 2 B). To improve the resolution even further, we performed structured illumination microscopy (SIM) on expanded cells (Figure 2 C). The result also demonstrated a largely continuous dextran signal between the nucleus and the kinetoplast, indicating the continuity of the endosomal structures.

To determine the expansion factor, the diameter of the flagellar pocket and the length of the endosomes were measured in multiple expanded and unexpanded cells (Figure 2 D). The median diameter of the fluorescence signal corresponding to the flagellar pocket increased from 0.84 µm to 3.08 µm, resulting in an expansion factor of 3.6. The median length of the endosomes increased from 2.51 µm to 7.88 µm, yielding an expansion factor of 3.1.

In summary, super-resolution microscopy using a transgenic marker cell line and cargo uptake assays supported the possibility that in trypanosomes endosomes are largely continuous.

298

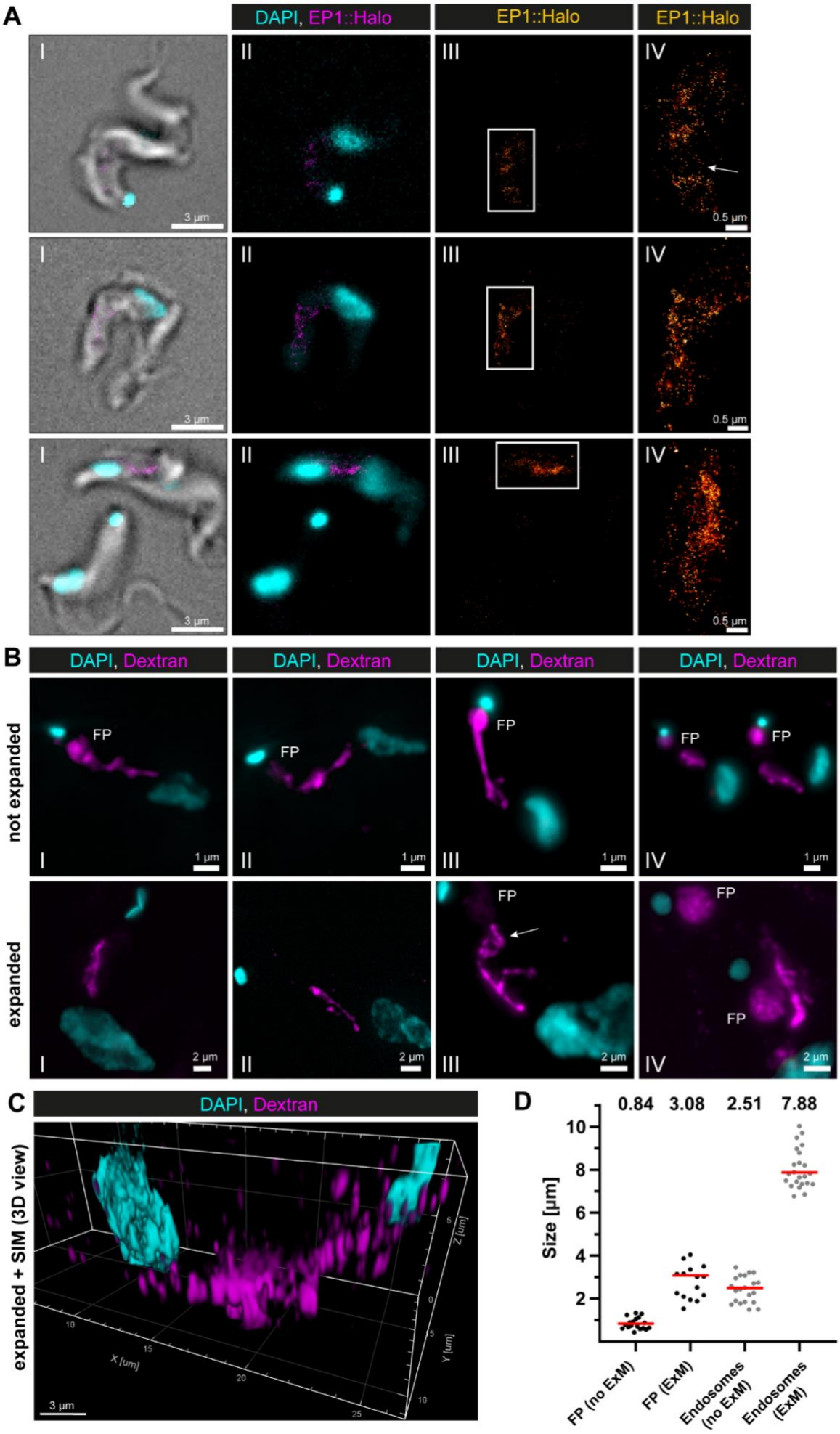
A
DAPI, EP1::Halo
EP1::Halo
EP1::Halo
I
II
III
IV
3 µm
0.5 µm
B
DAPI, Dextran
not expanded
expanded
FP
1 µm
2 µm
C
DAPI, Dextran
expanded + SIM (3D view)
X [um]
Y [um]
Z [um]
3 µm
D
0.84
3.08
2.51
7.88
Size [µm]
FP (no ExM)
FP (ExM)
Endosomes (no ExM)
Endosomes (ExM)

Figure 2. Super-resolution light microscopy reveals continuous endosomal membranes. (A) Visualisation of the endosomal system in *T. brucei* by direct stochastic optical reconstruction microscopy (*d*STORM). A transgenic EP1::HaloTag expressing bloodstream form cell line was generated and used to visualise the endosomal system. Cells were labelled with a HaloTag ligand and fixed with 4 % formaldehyde. Shown are a merge of transmitted light, DAPI staining and the EP1::HaloTag signal (I), a merge of DAPI staining and the EP1::HaloTag signal (II), the EP1::HaloTag signal (III) and a magnified view of the EP1::HaloTag signal (IV). **(B)** Visualisation of the endosomal system in *T. brucei* using expansion microscopy. Bloodstream form cells were pulsed with dextran conjugated to Alexa488 and fixed with 4 % formaldehyde and 0.2 % glutaraldehyde. Shown are exemplary images (I – IV) of not expanded and expanded cells imaged using widefield microscopy. All images represent a merge of DAPI staining (cyan) and dextran signal (magenta). Flagellar pockets (FP) are annotated. **(C)** 3D presentation of the endosomal system using a combination of expansion microscopy and structured illumination microscopy (SIM). The same gels as imaged in (B) were analysed with SIM. The 3D presentation was generated using the IMARIS package (Bitplane). **(D)** Scatter plot of the quantification of the expansion factor. The diameter of the fluorescence signal corresponding to flagellar pocket (FP) and length of the endosomes were measured in multiple not expanded (no ExM) and expanded cells (ExM) ($n \geq 15$). The median values are indicated as red bars and the corresponding numbers are shown in the upper part of the panel.

Quantitative 3D colocalization analysis reveals overlaps between early, late and recycling endosomal marker proteins

To functionally characterize different components of the endosomal system, specific antibodies against the endosomal marker proteins TbRab5A (early endosomes), TbRab7 (late endosomes), and TbRab11 (recycling endosomes) were generated and validated (Figure S2). Immunofluorescence assays were conducted, and the samples were imaged using 3D widefield microscopy. For quantitative colocalization analyses the previously established endosomal marker EP1::GFP (Engstler and Boshart, 2004) was used to define the entire endosomal compartment as the region of interest (ROI) (Figure 3).

The EP1::GFP fluorescence revealed a variable number of high intensity signals, surrounded, and connected by weaker signals (Figure 3 A, I). The fluorescence of the TbRab marker proteins was present in foci of varying numbers, sizes, and intensities (Figure 3 A, II – IV). The fluorescence signals for all three marker proteins were within the ROI defined by EP1. The visualization as maximum intensity projections (MIP) suggested that the different subdomains exhibited a low degree of colocalization and could represent physically distinct compartments for early, late, and recycling endosomes (Figure 3 A, V). To quantitate this finding, 3D objects were generated from the fluorescent signals for colocalization analysis using IMARIS (Figure 3 A, VI – X). These objects showed partial overlap. The pairwise colocalization of different endosomal markers is shown in Figure 3 A, XI - XIII and 3 B.

For the colocalization analysis, the EP1::GFP objects were masked and used as a 3D ROI in IMARIS. The colocalization matrix (Figure 3 C) showed that TbRab5A and TbRab7 exhibited the highest signal overlap, with approximately 53 % volume in both combinations. While 35 % of the volume of TbRab5A was colocalized with TbRab11, 26.5 % of the volume of TbRab11 was colocalized with TbRab5A. The differences in colocalization volumes can be attributed to the larger volume of the TbRab11 positive compartment. Similar observations were made for the combination of TbRab7 and TbRab11. While 45 % of the volume of TbRab7 was colocalized with TbRab11, 29.9 % of the volume of TbRab11 was colocalized with TbRab7. Furthermore, the different marker combinations yielded comparable moderate correlation coefficients (Pearson) ranging from 0.37 (TbRab5A and TbRab11) to 0.43 (TbRab5A and TbRab7) (Figure 3 D).

In summary, the quantitative colocalization analyses revealed that on the one hand, the endosomal system features a high degree of connectivity, with considerable overlap of

endosomal marker regions, and on the other hand, TbRab5A, TbRab7, and TbRab11 also demarcate separated regions in that system. These results can be interpreted as evidence of a continuous endosomal membrane system harbouring functional subdomains, with a limited amount of potentially separated early, late or recycling endosomes.

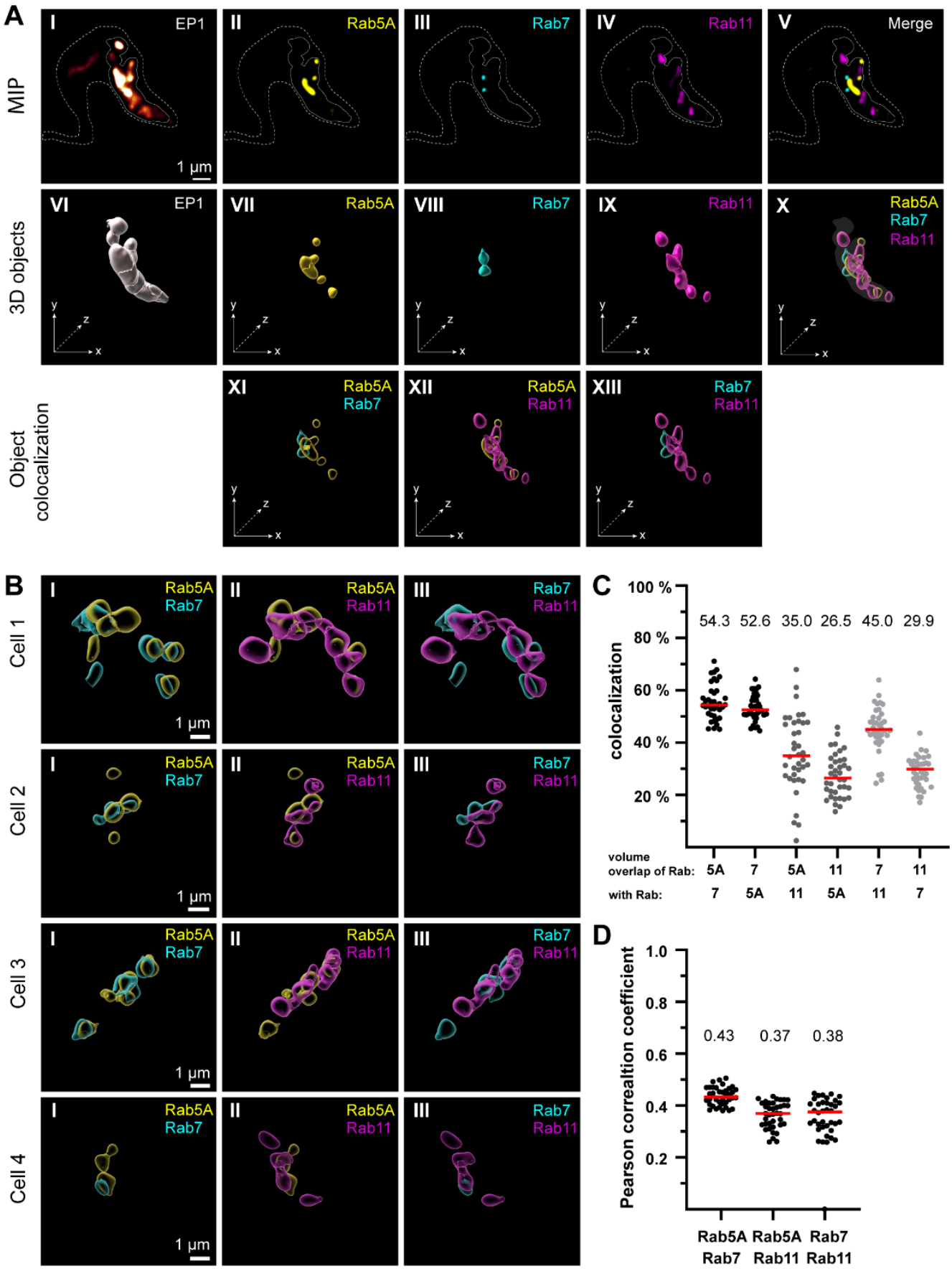
A
MIP
3D objects
Object colocalization
I EP1
II Rab5A
III Rab7
IV Rab11
V Merge
1 µm
VI EP1
VII Rab5A
VIII Rab7
IX Rab11
X Rab5A Rab7 Rab11
XI Rab5A Rab7
XII Rab5A Rab11
XIII Rab7 Rab11
B
Cell 1
Cell 2
Cell 3
Cell 4
C
colocalization
100 %
80 %
60 %
40 %
20 %
54.3 52.6 35.0 26.5 45.0 29.9
volume overlap of Rab: 5A 7 5A 11 7 11
with Rab: 7 5A 11 5A 11 7
D
Pearson correaltion coefficient
1.0
0.8
0.6
0.4
0.2
0.43 0.37 0.38
Rab5A Rab7
Rab5A Rab11
Rab7 Rab11

387

388

Figure 3. The endosomal markers TbRab5A, TbRab7, and TbRab11 partly colocalize in the posterior region of the cell. (A) The experimental workflow, from fluorescence images to object generation and quantitative 3D colocalization analysis, is exemplified. EP1::GFP (I) expressing cells were fixed and labelled with anti-TbRab5A (II), anti-TbRab7 (III) and anti-TbRab11 (IV) antibodies and imaged using widefield microscopy. Upper row: maximum intensity projections (MIP) for each individual fluorescence channel (I – IV) as well as a merge of all three anti-TbRab marker channels (V). The outline of the cell is shown by a dashed line (I - V) and the region of interest (endosomal system) is presented by a solid line (I - V). Middle row: Corresponding 3D objects to display the region of interest (VI) and the TbRab marker objects (VII – IX). The merge of all objects confirmed that the TbRab marker objects are located within the region of interest (X). Lower row: Colocalization of the objects representing TbRab5A and TbRab7 (XI), TbRab5A and TbRab11 (XII), TbRab7 and TbRab11 (XIII). The x-, y- and z-axes are indicated to support the three-dimensional view. **(B)** Object colocalization shown for additional cells. The colocalization of TbRab5A and TbRab7 (I), TbRab5A and TbRab11 (II), and TbRab7 and TbRab11 (III) is shown for different cells. (Cells 1 – 4). **(C - D)** Quantification of colocalization analysis for TbRab marker combinations. The colocalization function of IMARIS was used for the quantification. The EP1 surfaces defined the ROI (see panel A) and the automatic thresholding function (Costes et al., 2004) ensured minimal user bias. Each data point (n = 38) represents a field of view with 30 – 40 cells, corresponding to a total number of ~ 1,200 analysed cells. The median is highlighted with a red line and the corresponding number is written on top of the dataset. **(C)** Scatter plot of the colocalization analysis for the different TbRab marker combinations using the percentage of volume overlap. **(D)** Scatter plot of the colocalization analysis for the different TbRab marker combinations using the Pearson correlation coefficient.

The endosomal markers TbRab5A, TbRab7 and TbRab11 are present on the same membranes

To investigate the potential functional sub-compartmentalization of endosomes in trypanosomes, we conducted immunogold assays on Tokuyasu cryosections. We defined gold particles that were 30 nm or closer to a membrane as membrane-bound, considering a conservative calculation where two IgG molecules, each 15 nm in size, are positioned between the bound epitope and the gold particle (Figure 4, panel A). Consequently, gold particles located further away may represent cytoplasmic TbRab proteins or correspond to membranes that are not visible within the 55 nm thickness of the cryosection (Figure 4, panel C, arrows). The immuno-labelled structures exhibited a range of architectural features, including vesicular and tubular cisternae with circular or elongated shapes (Figure 4, 5, 6). The tubular structures had a thickness of 20 – 30 nm and extended up to a few microns in length (with the longest example shown in Figure 5, panel F, arrow). Vesicular shapes were observed in various sizes ranging from 30 nm to 135 nm in diameter.

While there were endosomal structures exclusively labelled with TbRab5A or TbRab7 (Figure 4 D, E, and G), a significant number of endosomal structures were labelled with both marker proteins (Figure 4, B - G). In contrast to TbRab5A and TbRab7, TbRab11 tended to form signal clusters on elongated structures (Figure 5 A, B, and D; Figure 6 D - F). TbRab11 was observed together with TbRab5A (Figure 5 A - F) or TbRab7 (Figure 6 A - G) on the same endosomal membranes, but it was also found as the sole marker on other endosomal membranes (Figure 5 B, D, F; Figure 6 C and G). The structures with a disk shape and positive for TbRab11 (Figure 5 F) were identified as exocytic carriers, as previously described in Grünfelder et al. (2003). Another noteworthy observation was that long elongated structures tended to have no or only weak labelling with any of the TbRab markers (Figure 5, panel F, arrow). To exclude potential artifacts, both gold size combinations were utilized for all marker combinations.

In summary, the exemplary images shown in Figures 4, 5 and 6 demonstrate the colocalization of TbRab5A, TbRab7 and TbRab11 on the same membranes, suggesting that the endosomal membrane system is unlikely to consist of distinct and independent compartments for early, late and recycling endosomes.

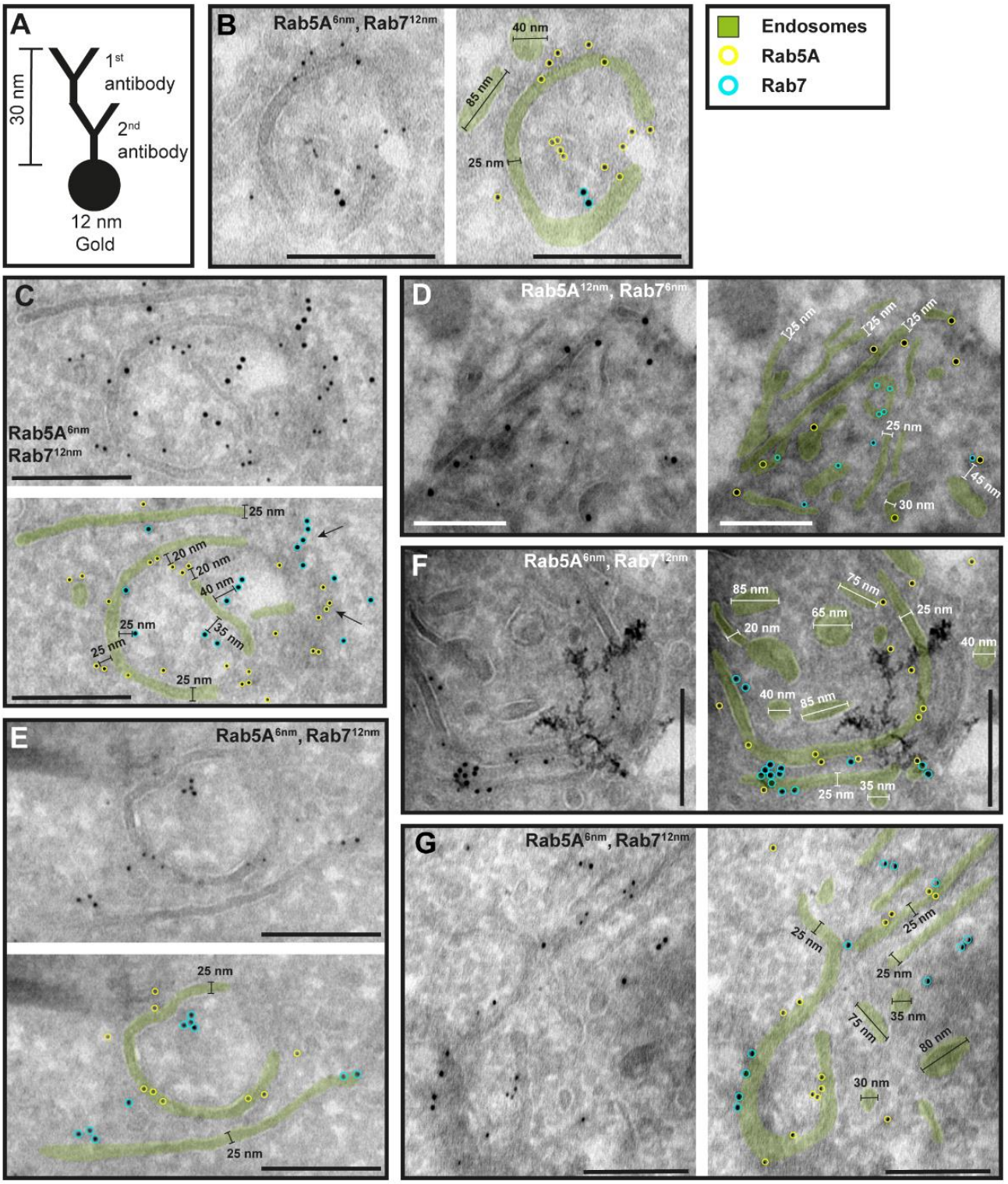

Figure 4. The endosomal markers TbRab5A and TbRab7 are present on the same membrane. (A) Schematic representation of antibody binding to visualise the maximum linkage error of 30 nm between a bound epitope and the gold particle. **(B - G)** Electron micrographs of cryosections labelled with rat anti-TbRab5A and guinea pig anti-TbRab7 antibodies and visualized with 6 or 12 nm gold-coupled secondary antibodies. For each panel an annotated and an unedited version of the image is presented. Endosomes are highlighted in green. Gold particles corresponding to TbRab5A signals are labelled in yellow. Gold particles corresponding to TbRab7 signals are highlighted in cyan. Scale bars: 200 nm.

459

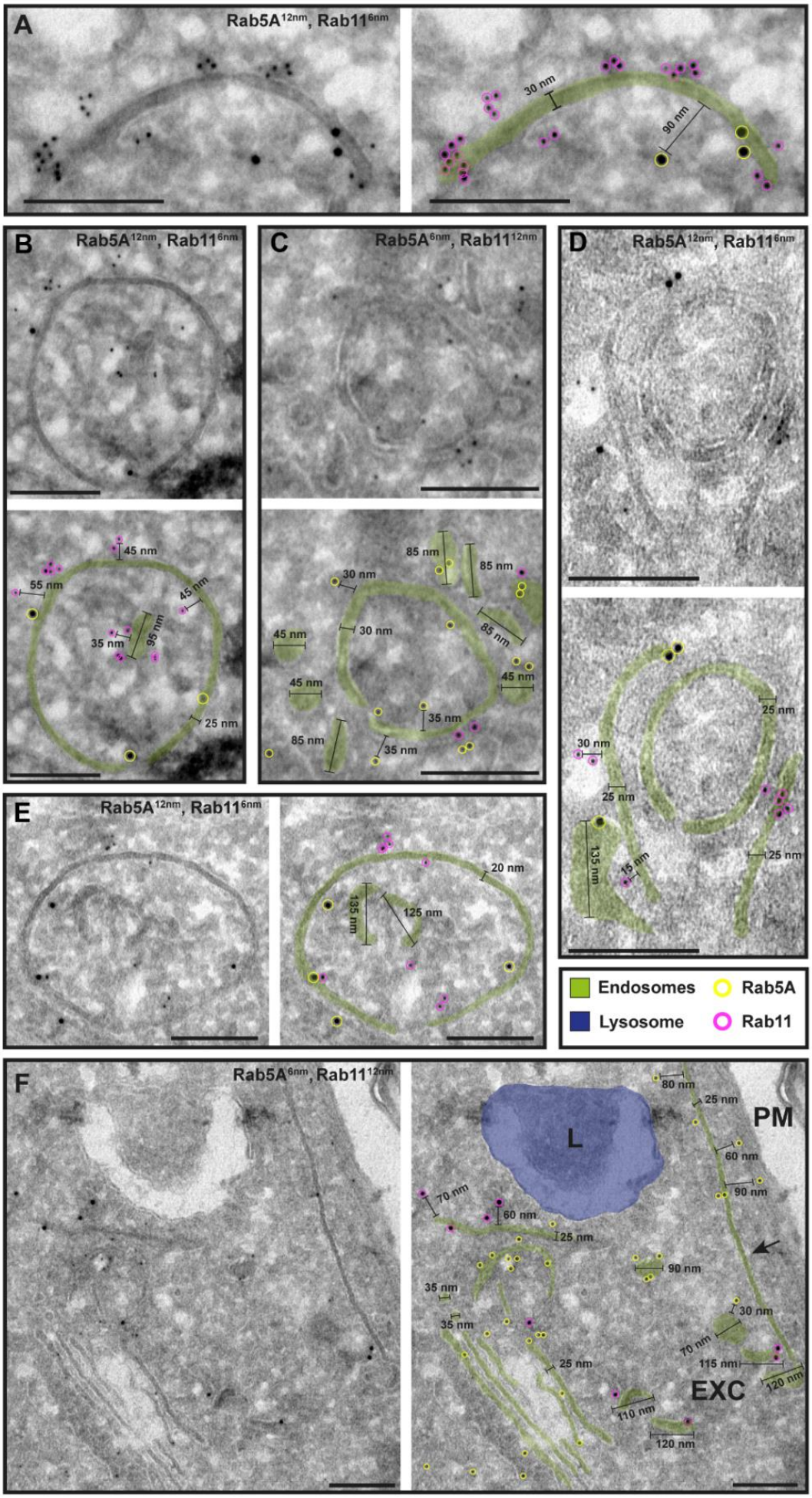
A
Rab5A12nm, Rab116nm
30 nm
90 nm
B
Rab5A12nm, Rab116nm
45 nm
55 nm
45 nm
35 nm
95 nm
25 nm
C
Rab5A6nm, Rab1112nm
85 nm
85 nm
30 nm
45 nm
30 nm
85 nm
45 nm
45 nm
35 nm
85 nm
35 nm
D
Rab5A12nm, Rab116nm
25 nm
30 nm
25 nm
135 nm
15 nm
25 nm
E
Rab5A12nm, Rab116nm
20 nm
135 nm
125 nm
Endosomes
Rab5A
Lysosome
Rab11
F
Rab5A6nm, Rab1112nm
80 nm
25 nm
PM
L
60 nm
90 nm
70 nm
60 nm
25 nm
90 nm
35 nm
30 nm
35 nm
70 nm
25 nm
115 nm
120 nm
EXC
110 nm
120 nm

Figure 5. The endosomal markers TbRab5A and TbRab11 are present on the same membranes. (A - F) Electron micrographs of cryosections labelled with rat anti-TbRab5A and rabbit anti-TbRab11 antibodies and visualized with 6 or 12 nm gold-coupled secondary antibodies. For each panel an annotated and an unedited version of the image is presented. Endosomes are marked in green, and the lysosome is highlighted in blue. Gold particles are marked in yellow (TbRab5A) and in magenta (TbRab11). Scale bars: 200 nm. Exocytic carrier (EXC), lysosome (L), plasma membrane (PM).

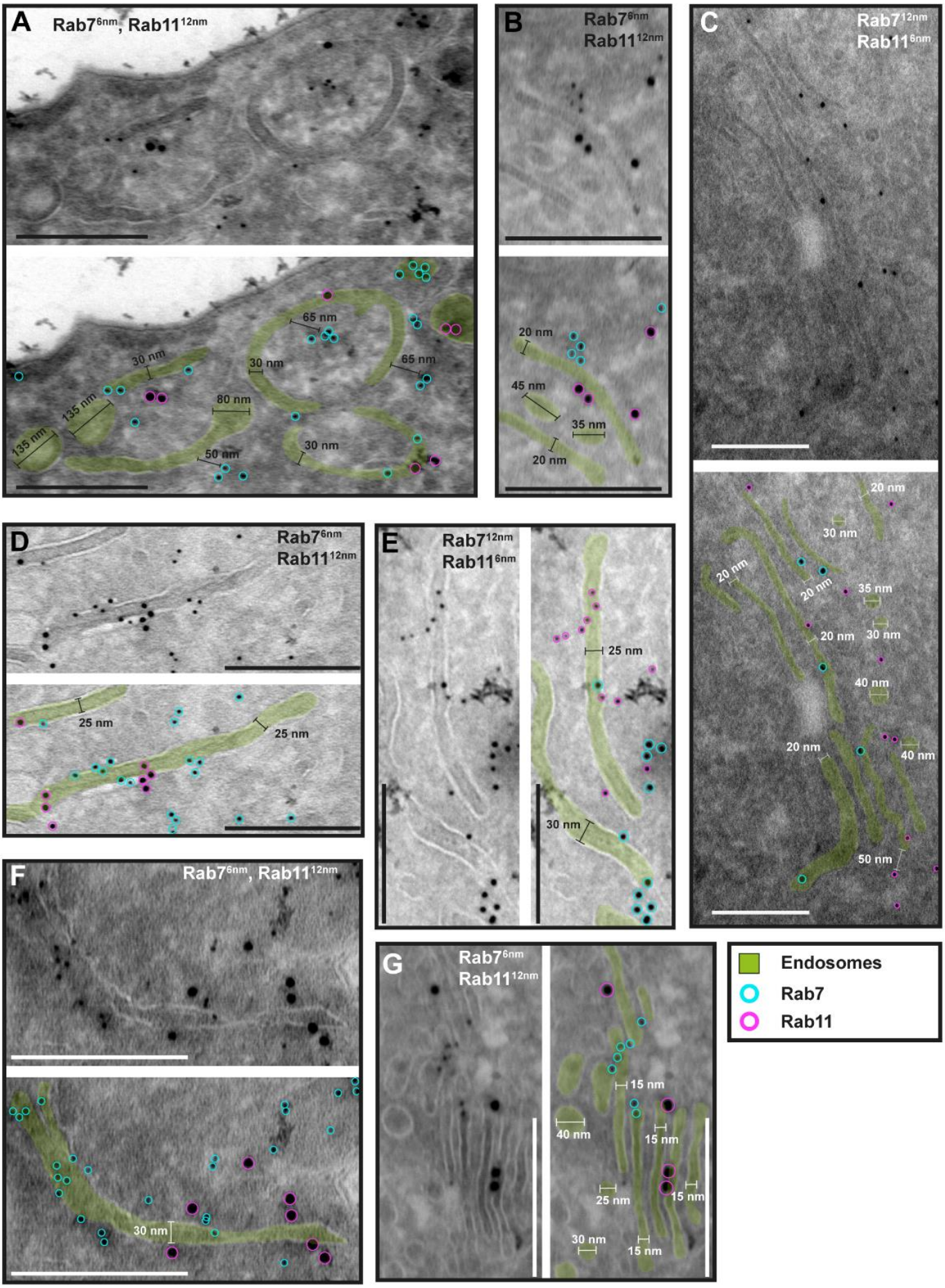
A
Rab7 6nm, Rab11 12nm
65 nm
30 nm
30 nm
65 nm
135 nm
80 nm
135 nm
50 nm
30 nm
B
Rab7 6nm
Rab11 12nm
20 nm
45 nm
35 nm
20 nm
C
Rab7 12nm
Rab11 6nm
20 nm
30 nm
20 nm
20 nm
35 nm
20 nm
30 nm
40 nm
20 nm
40 nm
50 nm
D
Rab7 6nm
Rab11 12nm
25 nm
25 nm
E
Rab7 12nm
Rab11 6nm
25 nm
30 nm
F
Rab7 6nm, Rab11 12nm
30 nm
G
Rab7 6nm
Rab11 12nm
15 nm
40 nm
15 nm
25 nm
15 nm
30 nm
15 nm
Endosomes
Rab7
Rab11

Figure 6. The endosomal markers TbRab7 and TbRab11 are present on the same membranes. (A - G) Electron micrographs of cryosections labelled with guinea pig anti-TbRab7 and rabbit anti-TbRab11 antibodies visualized with 6 or 12 nm gold-coupled secondary antibodies. For each panel an annotated and an unedited version of the image is presented. Endosomes are highlighted in green. Gold particles are labelled in cyan (TbRab7) and in magenta (TbRab11). Scale bars: 200 nm.

To confirm that the analysed membrane structures indeed represent endosomal membranes, we conducted cargo uptake assays and anti-VSG immunogold labelling (Figure 7). Trypanosomes were either pulsed with fluid-phase cargo (BSA; Figure 7, A - C) or cargo was taken up by receptor-mediated endocytosis (transferrin, Tf; Figure 7, D - F), and the sections were subsequently labelled with anti-TbRab antibodies. BSA and transferrin perfused the entire endosomal system, with the conjugated 5 nm gold particles visible inside the endosomal structures (Figure 7, A - F). Moreover, gold particles were observed within vesicles (Figure 7, B and D) and accumulated within the lysosome (Figure 7, A and B). In another set of experiments, the parasites were not pulsed with cargo markers, but the sections were labelled with anti-VSG and anti-TbRab antibodies (Figure 7, G - I). The anti-VSG antibodies decorated the entire plasma membrane (Figure 7, G) as well as intracellular membrane structures (Figure 7, G - I). The different TbRab marker proteins were found on the same membrane structures as the cargo markers or the anti-VSG antibodies (Figure 7, all panels). In summary, the use of cargo markers and antibodies targeting VSG and endosomal marker proteins confirmed the identity of the trypanosome endosomes.

555

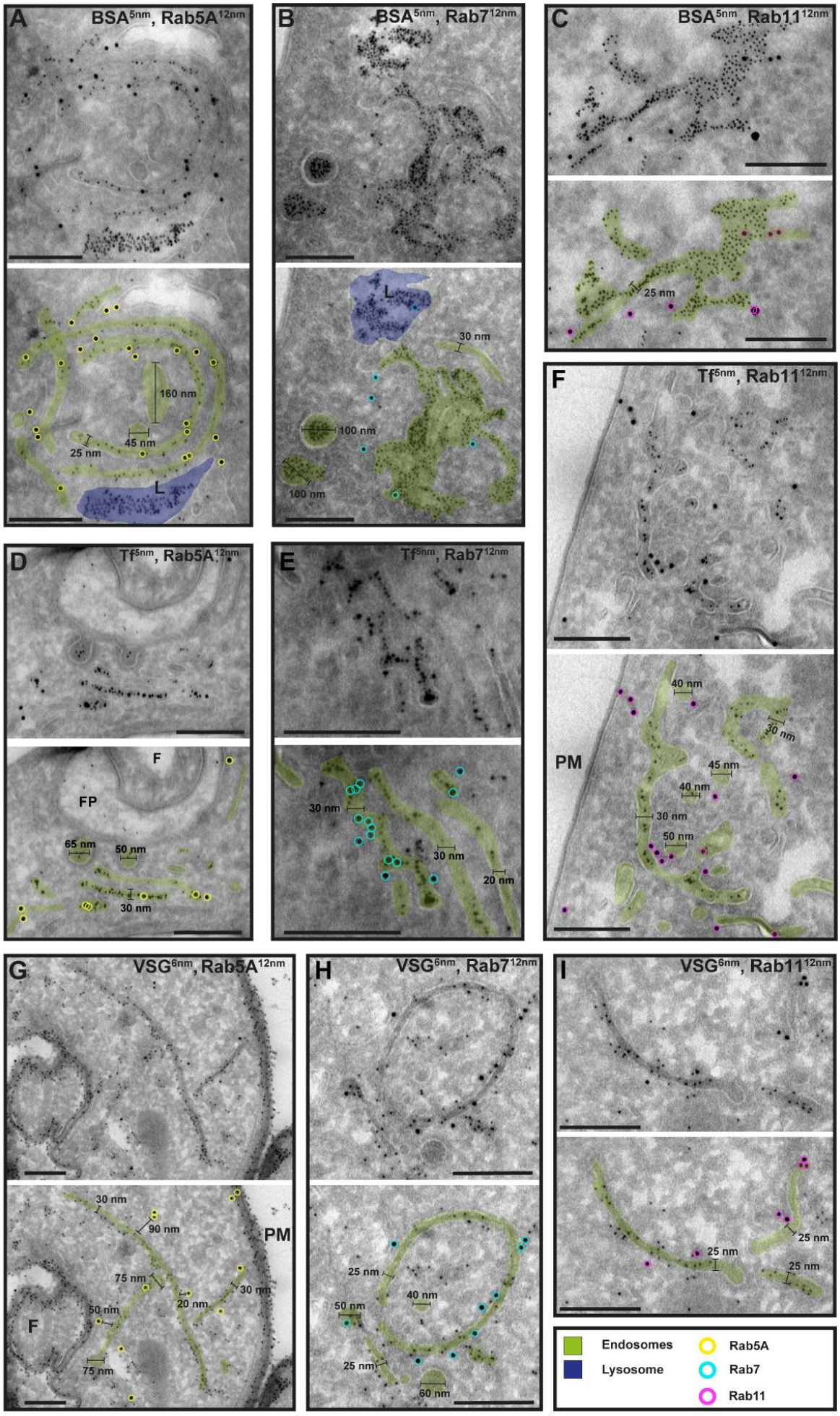
A
BSA5nm, Rab5A12nm
160 nm
45 nm
25 nm
L
B
BSA5nm, Rab712nm
L
30 nm
100 nm
100 nm
C
BSA5nm, Rab1112nm
25 nm
D
Tf5nm, Rab5A12nm
F
FP
65 nm
50 nm
30 nm
E
Tf5nm, Rab712nm
30 nm
30 nm
20 nm
F
Tf5nm, Rab1112nm
40 nm
30 nm
PM
45 nm
40 nm
30 nm
50 nm
G
VSG6nm, Rab5A12nm
30 nm
90 nm
PM
75 nm
30 nm
20 nm
50 nm
F
75 nm
H
VSG6nm, Rab712nm
25 nm
40 nm
50 nm
25 nm
60 nm
I
VSG6nm, Rab1112nm
25 nm
25 nm
25 nm
Endosomes
Lysosome
Rab5A
Rab7
Rab11

Figure 7. Cargo uptake and anti-VSG immunogold labelling confirm the endosomal identity. (A – I) Electron micrographs of cryosections labelled with anti-TbRab5A (yellow), anti-TbRab7 (cyan) or anti-TbRab11 (magenta) antibodies and 12 nm gold-conjugated secondary antibodies. For each panel an annotated and an unedited version of the image is presented. Endosomes are highlighted in green, the lysosome in blue. Parasites were incubated with 5 nm gold-conjugated BSA **(A – C)** or transferrin (Tf) **(D – F),** prior to fixation, sectioning and immunolabelling. BSA and transferrin cargo was observed in vesicles, endosomes, and lysosome. **(H – I)** Cells were labelled with anti-VSG antibodies and 6 nm gold-conjugated secondary antibodies. (F), flagellum, (FP) flagellar pocket, (PM) plasma membrane, (L) lysosome. Scale bars: 200 nm.

3D Tokuyasu proves that trypanosomes have continuous endosomal membranes

Following the visualization of continuous endosomal membranes through cargo uptake assays in Epon resin sections (Figure 1), we aimed to confirm these findings using 3D immuno-electron microscopy on cryosections (Figure 8). Cryosections with a thickness of 250 nm were labelled with antibodies against TbRab5A, TbRab7, and TbRab11. The 3D reconstructions provided an in-depth view of the interconnected circular and tube-like structures. Although the tomograms represented only a 250 nm thick section of a cell, it was evident that the membrane system likely exhibited further connections above and below the field of view. This assumption was confirmed by our experiments with conventional electron tomography. The 3D Tokuyasu method effectively highlighted the interconnectedness of these structures, expanding upon the observations from 2D analyses. We observed endosomes decorated with different TbRab signals, supporting our assumption that functional subdomains exist within the same endosomal membrane system (Figure 8, A II and III, B II). It is worth noting that smaller gold particles demonstrated better penetration of the cryosections, explaining the higher abundance of 6 nm gold particles compared to 12 nm gold particles. Another noteworthy finding was the presence of TbRab5A and TbRab7 in the lysosomal lumen, suggesting their possible degradation (Figure 8, A and B).

In addition, the endosomal membranes were juxtaposed to the trans-Golgi in all Tokuyasu tomograms, further implying a role of the endosomal system in post-Golgi trafficking (Figure 8, A I and B III). In summary, our second 3D electron microscopy approach successfully visualized the continuous membrane system of the endosomal apparatus in *T. brucei* and represents the first utilization of the advanced 3D Tokuyasu technique in trypanosomes.

612

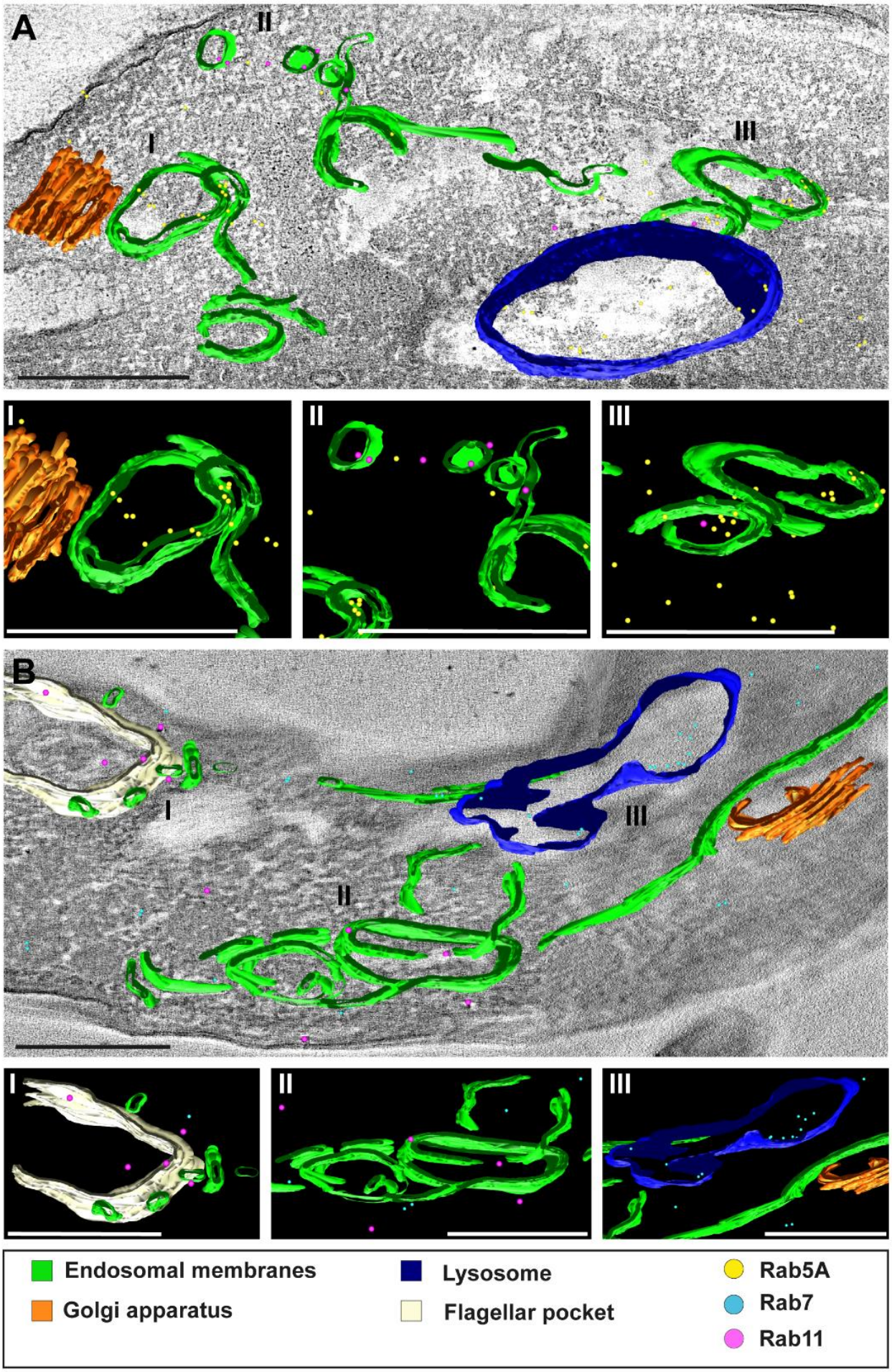
A
I
II
III
B
I
II
III
Endosomal membranes
Golgi apparatus
Lysosome
Flagellar pocket
Rab5A
Rab7
Rab11

Figure 8. 3D Tokuyasu confirmed continuous endosomal membranes in cryosections. (A, B) Tomographic reconstruction of the endosomal apparatus. **(I – III)** Isolated view of different organelle structures. Cryosections (250 nm) were labelled with anti-TbRab antibodies and 6 or 12 nm gold-coupled secondary antibodies. Endosomes are shown in green, lysosomes in blue, the flagellar pocket in white, the Golgi apparatus in orange. Gold particles are indicated as coloured spheres; TbRab5A (yellow), TbRab7 (cyan) or TbRab11 (magenta). Scale bars: 500 nm. Movies corresponding to panel A and B can be found here: A) z-stack, 3D model; B) z-stack, 3D model.

Discussion

Evolution has endowed African trypanosomes with a cellular multi-tool, the VSG-surface coat. Apart from exhibiting antigenic variation across hundreds of coat variants, the VSG proteins are attached to the cell surface through GPI-moieties, enabling their remarkable mobility. Exploiting this feature, the parasites evade early immune responses by clearing antibodies. This evasion process hinges upon the highly polarized nature of the trypanosome cell body, with exclusive endocytic uptake occurring at the posterior end, coupled with an exceptionally rapid membrane recycling rate. The prevailing model of the endosomal system, consisting of distinct compartments for early, late, and recycling endosomes, seems incompatible with the observed rapid turnover rates in *T. brucei*. Nevertheless, the parasite expresses the canonical Rab GTPases which serve as markers for these endosomal compartments, such as Rab5 (early), Rab7 (late), and Rab11 (recycling endosomes). To resolve this apparent contradiction, we performed a structure-function analysis of the trypanosome endosome apparatus.

3D electron tomography reconstructions, utilizing cargo uptake assays (Figure 1; Supplementary movie 1), revealed a complex network of endosomal structures in *T. brucei*. These compartments were characterized by interconnected fenestrated sheets, circular cisternae, and tubular structures, that formed a single intricate endosome. Our results shine a new light on transmission electron microscopic studies of the trypanosome endomembrane system (reviewed in Link et al., 2021). Based on 2D information the giant endosomal sheets had been interpreted as extended tubular structures, fenestrations as vesicles and the connective areas as irregularly shaped structures (Engstler et al., 2004; Grünfelder et al., 2003; Overath and Engstler, 2004).

In mammalian cells, tubular endosomes constitute a major part of the endosomal system. Tubules possess a higher surface area-to-volume ratio compared to vacuolar regions. As a result, they have been proposed to geometrically sort membrane-associated proteins over soluble cargo (Mayor et al., 1993). It is assumed that the carrier tubules, following detachment, transport their cargo either to the plasma membrane or to the recycling endosomes.

T. brucei lacks elongated tubulo-vesicular structures. Furthermore, our tomographic analysis did not reveal the conventional tubular carriers (reviewed in Chi et al., 2015). Instead, in these parasites, geometric sorting most likely occurs at the rims of flat, fenestrated sheets. A specific class of clathrin-coated vesicles (CCV II) pinches off from these strongly curved membrane

areas. They transport bulky fluid phase cargo and membrane protein complexes (such as VSG^{IgG}) to the lysosome (Engstler et al., 2004; Grünfelder et al., 2003).

The sorting mechanism into CCV II vesicles could be a purely physical process. Both the fenestrated sheets and circular cisternae exhibit the same inner width of about 35 nm. The VSG coat occupies 2 x 15 nm of this width, significantly limiting the available volume for fluid phase cargo. As the VSG concentration in the membrane increases, the bulky cargo is pushed towards the edges of the sheets, resulting in further membrane deformation that facilitates the recruitment of clathrin. The VSG is excluded from the CCV II and thus not transported to the lysosome. How this works mechanistically is unknown, however, it is tempting to speculate that the geometric sorting of larger cargo into the CCV II, sterically excludes VSG.

The electron tomographic analysis of the *T. brucei* endosome yielded compelling evidence of an extensive and interconnected membrane system. While this conclusion is supported by a substantial number of tomograms, the technique is not well suited for quantitative analyses.

Therefore, we conducted super-resolution microscopy and cargo uptake assays (Figure 2). The *d*STORM analyses verified that endosomal membranes in *T. brucei* likely form a continuous structure. Regions exhibiting higher signal density and intensity were consistently interconnected, small membrane bridges can however not be fully resolved, as the label density in these regions is not sufficient to grant structural resolution (Figure 2A, upper row, image IV, indicated by an arrow).

To analyse the full 3D volume of the cell, expansion microscopy was conducted (Figure 2 B - D). The visualised endosomal network looked like the elongated and circular structures found in the reconstruction of the electron tomograms (Figure 1). While the elongated structures could easily correspond to the fenestrated sheets (Figure 2 B), the circular structure (Figure 2 B, middle row, image III, arrow) nicely recapitulates the morphology of a circular cisternae (Figure 1 C). Interestingly, dividing cells (possessing two kinetoplasts and two flagellar pockets) always showed a fluorescence signal corresponding to the endosomal system juxtaposed only to the “old” flagellar pocket, indicating that the duplication of the endosomal network might occur *de novo* during the cell cycle. The 3D presentation (Figure 2 C) confirmed the continuity of the endosomal membranes, which had been seen already in the electron tomography.

In contrast to *d*STORM or SIM, expansion microscopy (ExM) offers a selective perspective on the trypanosome endosomal system. To date, ExM has been effectively employed to visualize

cell structures associated with the cytoskeleton or other stabilizing supports (Alonso, 2022; Amodeo et al., 2021; Gambarotto et al., 2019; Gorilak et al., 2021; Kalichava and Ochsenreiter, 2021). However, we could not find any published ExM images of endosomes. Our initial efforts to identify endosomal markers using ExM were also unsuccessful. Only when we added the inert fluid phase cargo dextran did the endosomes become clearly visible. This was likely due to the stabilizing effect of the cargo.

Having established that the endosomes in trypanosomes likely form a continuous cellular structure, our next inquiry was whether this would be evident in the simultaneous presence of the canonical marker proteins TbRab5A, TbRab7, and TbRab11. To define the region of interest in 3D immunofluorescence microscopy, we utilized the previously established fluorescent marker EP1::GFP (Engstler and Boshart, 2004), which stains the entire endosomal system. Maximum intensity projections (MIPs) of multichannel images indicated that the TbRabs were closely juxtaposed but in distinct endosomal compartments (Figure 3 A, upper row). This finding aligns with the results of a previously published quantitative colocalization analysis of TbRab5A and TbRab7 (Engstler et al., 2004). However, the presentation as 3D objects already implied an overlap between the different marker proteins. The present study now reveals that endosomal sheets can easily span over several micrometres, which fundamentally alters the interpretation of the light microscopy colocalization data. Thus, the seemingly separate structures could well be subdomains of the same membrane structure.

We therefore performed quantitative colocalization analyses with all marker combinations (Figure 3). The degree of colocalization was assessed by determining the percentage of overlap for the volume of one TbRab marker colocalized with another. Notably, TbRab5A and TbRab7 exhibited a significantly higher percentage of overlap (about 53 %) compared to the other marker combinations (Figure 3 C). An overlap of Rab5 and Rab7 has also been found in mammalian cells where it has been attributed to a temporary phenomenon during the maturation of early to late endosomes (Podinovskaia et al., 2021; Rink et al., 2005; van der Beek et al., 2021).

Interestingly, TbRab7 exhibited a higher degree of colocalization with TbRab11 (45 %) than TbRab5A showed with TbRab11 (35 %). This observation could indicate a functional polarization within the flagellar pocket. TbRab11 is known to decorate disk-shaped structures called exocytic carriers (EXCs), which transport the recycled VSG coat back to the cell surface. We suggest that the fusion of EXCs with the flagellar pocket membrane occurs specifically in a region marked by four specialized microtubules. Consequently, while clathrin-mediated

endocytosis to TbRab5A-positive membrane areas takes place everywhere on the flagellar pocket, exocytosis is limited to a subdomain of the pocket (Supplementary movie 2). This disparity explains the lower colocalization between TbRab11 and TbRab5A. It is worth noting that the mechanism by which Golgi-derived membrane and cargo are transported to the flagellar pocket in trypanosomes remains unclear. In our view, the most plausible scenario involves feeding into the rapid endocytic recycling pathway, which is further supported by the absence of tubular carriers as observed in mammals.

Quantitative colocalization analysis by 3D IF provides statistically valid results, however, has the obvious limitation that it lacks ultrastructural information. Therefore, we analysed the localization of the different TbRab proteins on cryo-electron micrographs. This finally proved that different TbRab markers can be found on the same membrane structures and argues against the existence of distinct early, late, and recycling endosomal compartments in *T. brucei* (Figures 4, 5 and 6). An alternative explanation for the two marker proteins residing on the same membrane would the endosome maturation model, which has been proposed in mammals (Poteryaev et al., 2010; Rink et al., 2005; Stoorvogel et al., 1991). In short, early endosomes undergo maturation and transform into late endosomes through a series of changes. This maturation process involves the acquisition of new membrane proteins and enzymes that among others facilitate a decrease in the pH value. Ultimately, the late endosomes fuse with lysosomes, leading to cargo degradation (reviewed in Podinovskaia and Spang, 2018).

EM-cryosections provide high-resolution 2D information. To gain volume information, we resorted to an extremely demanding technique that combines ultrastructural 3D information with immunodetection. 3D Tokuyasu has not been applied to trypanosomes and the utilisation of 3D immunogold has not been used on endosomes in any system. The Tokuyasu tomograms clearly showed the connection of circular cisternae and sheet-like structures in 3D (Figure 8). The decoration with different endosomal marker proteins proved the existence of functional subdomains within a giant endosomal membrane system convincingly, and finally offered an explanation to the fundamental question of how trypanosomes can combine endosomal functionality with very fast membrane recycling.

Our work has certainly raised more questions than it has answered. One puzzling aspect is the presence of extended sheet-like endosomal structures that display sparse or no labelling of TbRab proteins. This is particularly intriguing when considering the substantial membrane area covered by these sheets. It is tempting to speculate that the absence of canonical markers correlates with a lack of endosomal function. We postulate that these sheets represent

"endosomal highways" that support fast flow of cargo by facilitated diffusion. This may allow for the efficient transport of VSG and fluid-phase cargo between distinct functional endosomal subdomains, which can be in close proximity or at a distance of microns apart. Consequently, the slow vesicular trafficking process in trypanosomes could be limited to clathrin-coated vesicles, originating either from the flagellar pocket or the rims of fenestrated sheets and cisternae, as well as to Rab11-positive exocytic carriers.

Interestingly, we did not find any structural evidence of vesicular retrograde transport to the Golgi. Instead, the endosomal 'highways' extended throughout the posterior volume of the trypanosomes approaching the trans-Golgi interface. It is highly plausible that this region represents the convergence point where endocytic and biosynthetic membrane trafficking pathways merge. The presence of fluid-phase cargo within the endosomal sheets strongly contradicts the possibility of these sheets representing the trypanosome trans-Golgi network (TGN). The absence of evidence for a TGN is not the only peculiarity of the trypanosome Golgi. A canonical ER-Golgi-intermediate-compartment (ERGIC) with tubulo-vesicular clusters is also absent. Our electron tomographic analyses revealed that the coat protein II (COP II) vesicles at the ER-Golgi interface have a diameter of 60 nm and hence are equivalent to so-called regular COP II vesicles in mammalian cells (Supplementary movie 3). All other COPII vesicle types seem to be missing in *T. brucei* (Mironov et al., 2003; Mogelsvang et al., 2003). All this could point to a reduced control of ER-to-Golgi traffic. We propose that trypanosomes have shifted the central orchestrating function of the TGN as a sorting hub at the crossroads of biosynthetic and recycling pathways to the endosome.

In summary, we confirmed the endosomal identity of the analysed membranes with the aid of cargo uptake assays (Figure 1, 2 and 7), transgenic cell lines (Figure 2 and 3) as well as immuno labelling (Figure 3 - 8) combined with various light and electron microscopy methods. In the process, we ensured that all examined membranes belonged to the endosomal system and we did not, for example, mischaracterize ER membranes as endosomal membranes. All our results suggest that the endosomal apparatus consists of a continuous membrane system with TbRab5A, TbRab7 or TbRab11 positive subdomains that can be dynamically formed (Figure 9). Thus, the overall architecture of the trypanosome endosomes represents an adaptation that has facilitated the extreme speed of plasma membrane recycling observed in these organisms.

A partially continuous endosomal membrane structure has been proposed in the South American parasite *Trypanosoma cruzi* (Alcantara et al., 2018; Porto-Carreiro et al., 2000), however, no endosome markers were used in that study to corroborate their findings. In the

single-celled parasite *Giardia*, the peripheral vesicles that constitute the endosomal organelles form an “interconnected network” (reviewed in Benchimol and de Souza, 2022), while the endosome-like compartment in *Toxoplasma* is likely involved in both endocytic and exocytic trafficking (reviewed in McGovern et al., 2021). In *Leishmania,* the endosomal system has not been fully characterized but seems to be under physical tension (reviewed in Ansari et al., 2022). Thus, parasitic protozoa might feature interesting variations of the common cell biological process of endocytosis. Furthermore, these variations might extend to many other organisms beyond the extensively studied, yet not entirely representative model organisms. The emergence of technologies such as CRISPR and single-cell analyses now enables the systematic exploration of the vast diversity of eukaryotic cells. Therefore, the systematic investigation of the phylogeny of cell biological inventions could be a logical next step.

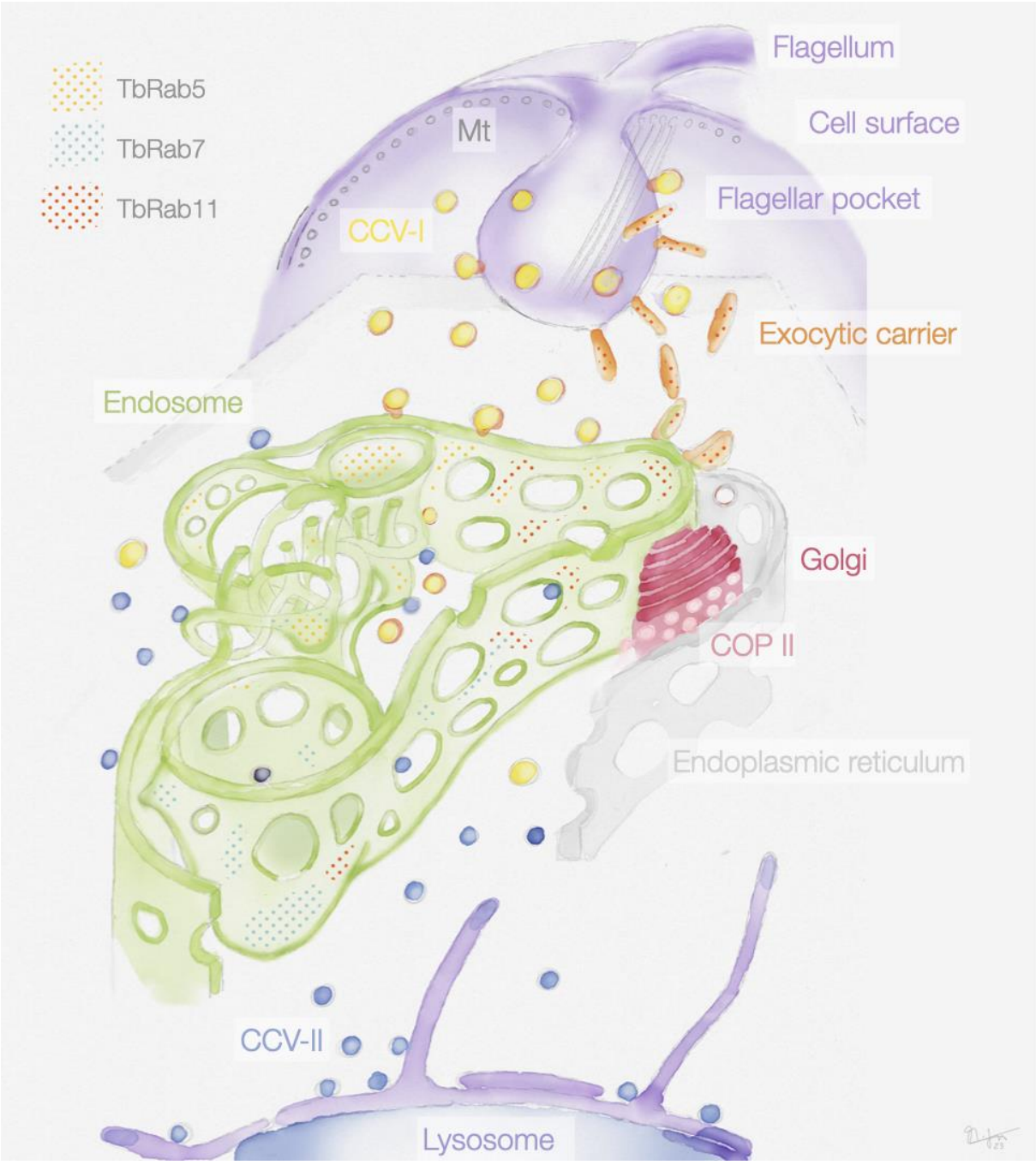

Figure 9. Schematic representation of the endosomal system in *T. brucei*. The endosome is marked by the presence of small GTPases of the Rab family: Rab5A (yellow dots), Rab7 (cyan dots), and Rab11 (red dots). Class I clathrin-coated vesicles (CCV-I), class II clathrin-coated vesicles (CCV-II), vesicles coated with coat protein (COP) II.

Material and methods

Cell culture and cell lines

T. brucei bloodstream-form parasites (Lister strain 427, antigenic type MITat 1.2, clone 221) were cultured in HMI-9 medium (Hirumi and Hirumi, 1989) supplemented with 10 % heat-inactivated foetal calf serum (Sigma-Aldrich), 100 U/ml penicillin and 0.1 mg/ml streptomycin. The cells were maintained at 37 °C and 5 % CO_2 split at regular intervals to keep the population densities below 1 x 10^6 cells/ml. Population density was monitored using a Z2 Coulter Counter (Beckman Coulter). The monomorphic "13-90" parasites expressing the T7 RNA polymerase and tetracycline repressor were cultivated in the presence of 5 µg/ml hygromycin and 2.5 µg/ml G418 (Wirtz et al., 1999). The transgenic bloodstream form "2T1" cells which constitutively express a T7 RNA polymerase and tetracycline repressor were cultivated in the presence of 2.5 µg/ml phleomycin and 1 µg/ml puromycin (Alsford et al., 2005). The RNAi cell lines (RNAi-TbRab5A, RNAi-TbRab7, RNAi-TbRab11) were based on the 2T1 cell line and cultivated in the presence of 5 µg/ml hygromycin and 2.5 µg/ml phleomycin. The transgenic EP1::GFP cells were based on MITat1.2 expressing wild type cells and cultivated in the presence of 5 µg/ml hygromycin and 15 µg/ml G418 (Engstler and Boshart, 2004). The transgenic single marker (SM) cell line (Wirtz et al., 1999) which constitutively express a T7 RNA polymerase and tetracycline repressor were cultivated in the presence of 2.5 µg/ml G418. The EP1::Halo tagged cell line was based on SM cells and was cultivated in the presence of 2.5 µg/ml phleomycin and 2.5 µg/ml G418.

Generation of RNAi cell lines

The RNAi target sequences were selected by entering the target gene ORF into the RNAit webapp (Redmond et al., 2003). The selected primer pairs flanked the base pairs 29 – 614 (TbRab5A), 134 – 630 (TbRab7) or 67 – 496 (TbRab11) and encoded the attB-sequence at the 5' end for the ligation into the pGL2084 plasmid (Jones et al., 2014). The plasmids were linearized with AscI and 10 µg were transfected into 3 x 10^7 mid-log phase bloodstream 2T1 cells (Alsford et al., 2005) using Amaxa Basic Parasite Nucleofector Solution 1 using the X-001 program of an Amaxa Nucleofector II (Lonza, Switzerland). Clones were selected by growth in medium containing phleomycin (2.5 µg/ml) and hygromycin (5 µg/ml).

Generation of EP1::Halo cell line

The insert for the EP1::HaloTag cell lines was generated in resemblance to the GFP::EP1 cell line from Engstler and Boshart (2004). For this, the Halo tag was inserted in between the N-terminal EP1 globular domain and the C-terminal EP1 stalk domain. The three fragments (EP1 globular domain, Halotag, EP1 stalk domain) were amplified using PCR. For the EP1 fragments, the GFP::EP1 plasmid was used (Engstler and Boshart, 2004). While amplifying the globular domain, an internal BamHI restriction site was removed by silent point mutation. The Halo tag sequence was amplified from the pFC20A (HaloTag®) T7 SP6 Flexi® vector (Promega, USA). All amplified fragments were then combined using Gibson assembly (Gibson assembly cloning kit, NEB) with 20 base pair overhangs. This construct was cloned into pJet1.2blunt and later excised using HindIII and BamHI for ligation into the pLew100v5 expression vector (Wirtz et al., 1999). For transfection of the parental, SM cell line, 10 µg of the NotI linearized plasmid was transfected. Clones were selected by growth in medium containing phleomycin (2.5 µg/ml) and G418 (2.5 µg/ml). Primers used: forward primer globular domain (AGTAAAATTCACAAGCTTGG ATGGCACCTCGTTCCCTTTATCTGCTCGCTGTTCTTCTGTTCAGCGCGAACCTCTTC GCTGGCGTGGGATTTGCCGCAGCCGCTGAAGGACCAGAAGACA), reverse primer globular domain (CCGATTTCTGCCAT TCTAGAGGTGGCGACCGGCCGGTGAATCCCGCCGACCTTGGTTCCCTTCTCGCCTT TGCCTTTGCCTCCCTTAGTAAGACCCTTGTCTTCTGGTCCTTCAGCGGCT), forward primer Halo tag, (TCTAGA ATGGCAGAAATCGGTACTGGCTTTCCATTCG), reverse primer Halo tag (TCAGTGCCATTGGTATCGTCCTTAATT AACCCGGAAATCTCCAGAGTAGACAGCC), forward primer stalk domain (TTAATTAA G GACGATACCAATGGCACTGACC), reverse primer stalk domain (AAAAGCCAACTAAATGGGCA GGATCC TTAGAATGCGGCAACGAGAGC).

Growth curves

Cells were seeded with a starting concentration below 1 x 10^6 cells/ml in a volume of 10 ml and divided into two 2 ml aliquots in separate wells of a 24-well plate. Tetracycline was added to a final concentration of 1 µg/ml in one well to induce RNAi or EP1::Halo expression. The population density of the non-induced and induced cells was determined every 24 h over a time course of 96 h, using a Z2 Coulter Counter (Beckman Coulter). Depletion of the target protein was confirmed by immunoblotting of whole-cell lysates (Supplements 2).

Cargo uptake

Per assay the same number of cells (1 x 10^7 for light microscopy, 1 x 10^8 for electron microscopy) were harvested by centrifugation (1500 x *g*, 10 min, 4 °C). After that, cells were washed with 1 ml TDB (5 mM KCl, 80 mM NaCl, 1mM $MgSO_4$, 20 mM Na_2HPO_4, 2 mM NaH_2PO_4, 20 mM glucose, pH 7.6), harvested by centrifugation (1500 x *g*, 2 min, 4 °C) and the supernatant was discarded. Next, the cells were resuspended in 100 µl TDB and incubated with either dextran-Alexa488 (light microscopy), transferrin-gold conjugates or BSA-gold conjugates (electron microscopy) for 15 min at 37 °C or HRP/ferritin for 5 min at 37 °C (electron microscopy). The final concentration of both dextran (ThermoFisher cat. number: D22910) and HRP (horseradish peroxidase type II, Sigma) was 10 mg/ml. The final concentration of ferritin (horse spleen ferritin, type I, Sigma) was 50 mg/ml. Transferrin-gold (Cytodiagnostics) or BSA-gold (Alexa555-BSA-Au, UMC Utrecht) were added to a final OD = 5. The uptake reactions were stopped by adding 1 ml of the corresponding fixatives (4 % formaldehyde and 0.2 % glutaraldehyde for the dextran uptake, 2 % formaldehyde and 0.2 % glutaraldehyde for BSA and transferrin uptake, 2.5 % glutaraldehyde for HRP uptake, 2 % formaldehyde and 1 % glutaraldehyde for ferritin uptake). Cells were fixed for 20 min on ice followed by 30 min at RT (for dextran uptake), 1 hour at RT (for HRP and ferritin) or 2 hours at RT (for BSA and transferrin uptake). Following this, cells were treated either as described in the immunofluorescence section or as explained in the sample embedding and immuno-electron microscopy section.

EP1::Halo cell labelling

Cells were harvested (1400 x *g*, 10 min, 37 °C) and washed in 1 ml TDB. The cell pellet was resuspended in 100 µl fresh TDB and HaloTag ligand (either in-house labelled Alexa647 ligand or Halo-Tetramethylrhodamine (TMR, Promega, USA) was added to a final concentration of 500 nM (Alexa647) or 5 nM (TMR). The labelling reaction was performed for 15 min at 37 °C and stopped by the addition of 4 % formaldehyde in PBS.

Immunofluorescence

Cells were harvested (1400 x *g*, 10 min, 37 °C), washed in ice-cold TDB, and fixed with 4% formaldehyde overnight (4 °C) or for 1 hour at RT. Fixed samples were washed in 1 ml PBS, harvested (1400 x *g*, 90 sec, RT) and 1 x 10^6 cells were added to each Ø 12 mm coverslip coated with 0.01 % poly-L-lysine (> 20 min, RT). The cells were attached to the coverslips by

centrifugation (750 x *g*, 1 min, RT) and attachment was confirmed visually. The attached cells were then permeabilized in 0.25 % Triton X-100 in PBS (5 min, RT) and blocked in 3 % (w/v) BSA in PBS (30 min, RT). Sequentially, coverslips were incubated with primary antibodies (1 h, RT), washed with PBS (3 x 5 min), and incubated once more with secondary antibodies (1 h, RT, in the dark). Finally, samples were washed in PBS (3 x 5 min), rinsed in ddH_2O, carefully dried, and mounted on glass slides using ProLong™ Diamond Antifade (Life Technologies). Antibodies were diluted in 1 % (w/v) BSA in PBS as follows: rat anti-TbRab5A 1:250, guinea pig anti-TbRab7 1:250, rabbit anti-TbRab11 1:250, goat anti-rat conjugated with Alexa Fluor 647 1:500, goat anti-guinea pig conjugated with CF568 1:500, goat anti-rabbit conjugated with Alexa Fluor 405 1:500.

Expansion microscopy

The proExM method was performed as described in (Tillberg et al., 2016) with some modifications. Approximately 1 x 10^7 cells were harvested by centrifugation (1500 x *g*, 10 min, 4 °C), then washed with 1 ml TDB, harvested by centrifugation (1500 x *g*, 2 min, 4 °C) again, and the supernatant was discarded. Next, the cells were resuspended in 100 µl TDB and incubated with dextran-Alexa488 for 15 min at 37 °C. The final concentration of dextran (ThermoFisher cat. number: D22910) was 10 mg/ml. The reaction was stopped by adding 1 ml 4 % formaldehyde and 0.2 % glutaraldehyde in PBS. Cells were fixed for 20 min on ice followed by 30 min at RT. After the fixation, cells were adhered to 12 mm coverslips. For anchoring of proteins, a solution of 5 mg AcX (A20700, Invitrogen), dissolved in freshly opened 500 µl anhydrous DMSO (D12345, Invitrogen), was prepared. A 100 µl drop of AcX 1:100 in PBS was placed on parafilm in a humidity chamber, the coverslips were inverted and incubated at room temperature for 16 hours. Coverslips were returned to a 24-well plate, washed twice for 5 minutes with PBS and stored in the fridge until the end of the day. For gelation, gelling solution was made mixing 100 µl monomer solution with 0.5 µl 10 % (v/v) APS and 0.5 µl TEMED, vortexed and used straight away. A volume of 50 µl was placed on a piece of parafilm in a humidity chamber and the coverslips were inverted and incubated at 37 °C for one hour. Monomer solution was prepared with sodium acrylate 8.6 % (w/v) (408220, Sigma), acrylamid 2.5 % (w/v), N-N'-methylenebisacrylamide 1.5 % (w/v) (M7279, Sigma) and NaCl 11.7 % (w/v) (AM9760G, Ambion) in PBS. Sodium acrylate stock solution 33 % (w/v) was prepared by dissolving 1.9 g in 5 ml of ddH_2O, 0.2 mm-filtered and used freshly. After polymerization, coverslips with the gel stuck to it were transferred to a 6-well plate with 1 ml of digestion solution (0.5 % Triton X100, 1 mM EDTA, pH 8 (AM9260G, Ambion), 50 mM

Tris, pH 8 (AM9855G, Ambion) and 1 M NaCl (AM9760G, Ambion) freshly supplemented with 10 U/ ml proteinase K (P8107S, New England Biolabs). Plates were slightly tilted to ensure the coverslip was completely covered and incubated at room temperature overnight. The next day, gels were detached from the coverslips and transferred to a Petri dish. After three rounds of expansion with 20 ml ddH_2O for 30 minutes each, gels were mounted in a poly-D-lysine coated imaging chamber (Nunc 155360 Lab-Tek II Chambered Coverglass with Cover, No. 1.5 Borosilicate Sterile) and imaged using a DMi8 widefield microscope.

Fluorescence microscopy

Images were acquired using a DMi8 widefield microscope (Thunder Imager, Leica Microsystems, Germany) with a HCX PL APO CS objective (100 x oil-immersion, NA 1.4, working distance 90 µm) and Type F Immersion Oil (refractive index = 1.518, Leica Microsystems, Germany). The microscope was operated using LAS-X software (Leica). Samples were illuminated with an LED8 light source (Leica) and 50 % illumination power. Excitation light was selected by using following filter sets: 391/32 nm; 479/33 nm; 554/24 nm; 638/31 nm (Leica Microsystems, Germany). Emitted light was collected at 435/30 nm (DAPI and Alexa Fluor 405), 519/25 nm (Dextran-Alexa Fluor 488 and GFP), 594/32 nm (CF568 and TMR) and 669 nm (Alexa Fluor 647), respectively. The individual exposure times were as follows: DAPI, Alexa Fluor 405, CF568, Alexa Fluor 647 = 200 ms; GFP = 500 ms; Dextran-Alexa Fluor 488 = 2 s; TMR = 2 s. Differential interference contrast (DIC) was used to visualise cell morphology. 3D recording of each field of view was obtained using 48 z-slices (step size = 0.21 µm). Fields of view were selected based on DIC to subjectively select for areas containing enough cells and blind the user to the fluorescence signal of the protein markers of interest. Images were captured using a Leica K5 sCMOS camera (pixel size 6.5 µm). The LAS-X/ Thunder integrated instant computational clearing (ICC) algorithm was used to remove background signal, using a minimal structure size of 338 nm.

Colocalization analysis

Widefield microscopy images were deconvolved using Huygens Essential version 21.10 (Scientific Volume Imaging B.V., Hilversum, Netherlands) and analyzed with IMARIS (9.9.1, Oxford Instruments). In brief, surfaces were rendered for the EP1 signal, and checked manually for accurate posterior localization in morphologically intact cells. These EP1 surfaces were used to define the ROI for colocalization analysis. The automatic thresholding function (Costes et

al., 2004) was used to ensure objective thresholding for the colocalization analysis of the different TbRab marker protein combinations.

*d*STORM imaging

Direct stochastic optical reconstruction (*d*STORM) imaging was performed on an inverted wide-field microscope (Olympus, IX-71). HaloTag-Ligand Alexa Fluor 647 was excited by a 641 nm diode laser (Topica, iBeam smart 640-S), a 405 nm diode laser (Coherent, Cube 405-100C) was used for DAPI excitation. Both Lasers were spectrally cleaned with cleanup filters (Chroma, laser clean up filter 640/10 & 405/20) and focused on the back focal plane of a 60x oil-immersion objective (Olympus, 60x NA 1.45). Emission light was separated from excitation light using a dichroic beam splitter (Semrock, FF410/504/583/669) and further spectrally filtered by a long-pass filter (Semrock, 647 nm RazorEdge). Images were recorded on an EM-CCD camera chip (Andor, iXon DU-897) with a measured pixel size of 134 nm. *d*STORM imaging was performed in a buffer of 100 mM MEA (Sigma-Aldrich, #M6500) in PBS at pH 7.4. Time series of 15 000 frames at an exposure time of 20 ms were captured while irradiating the sample by highly inclined laminated optical sheet (HILO) illumination with an intensity of approx. 2 kW cm^{-2}. Super-resolved images were reconstructed with rapidSTORM 3.3 (Wolter et al., 2012) and further processed for illustrations in Fiji. Widefield images of transmitted light and DAPI staining were captured after *d*STORM. For illustrations, the scale of the widefield images was matched to the super-resolved *d*STORM images.

SIM imaging

Structured Illumination imaging was performed using a Zeiss Elyra 7 lattice SIM equipped with a 63x C-Apochromat 63x/1.20 W (Zeiss) water immersion objective, four excitation lasers (405 nm diode, 488 nm OPSL, 561 nm OPSL, and 642 nm diode laser) and two sCMOS (PCO, pco.edge 4.2) cameras. Four-fold expanded gels were transferred onto PDL coated single well chamber slides (CellVis, #C1-1.5H-N). For excitation of DAPI the 405 nm laser diode was set to 10 % output power, for excitation of Dextran-Alexa488 the 488 nm laser to 20 %. A respective exposure time of 100 ms and 200 ms was set for the two channels. Z-stacks were captured in 3D Leap mode with optimal step intervals and appropriate filter sets (BP 420-480 + LP 655 and BP 495-550 + BP 570-620 for the DAPI- and 488-channel, respectively). SIM imaging was performed by capturing 13 phase-shifts of the lattice SIM pattern per slice. Super-

resolved images are processed in ZEN 3.0 SR FP2 (black) (Zeiss, Version 16.0.10.306) with SIM and SIM² processing modules.

Sample embedding and preparation for electron microscopy

For Tokuyasu immuno-EM, sample preparation and sectioning were performed as previously described (Engstler et al., 2004; Grünfelder et al., 2003; Möbius and Posthuma, 2019; Slot and Geuze, 2007). In short, 1 x 10^8 cells were harvested (1500 x *g*, 10 min, 37 °C) and washed with 1 ml TDB. Cells were fixed by addition of 4 % formaldehyde and 0.4 % glutaraldehyde in 0.2 M PHEM buffer (120 mM PIPES, 50 mM HEPES, 4 mM $MgCl_2$, 20 mM EGTA adjusted to pH 6.9 with 1 M NaOH) 1:1 to TDB. After 5 min the fixatives were replaced with 2 % formaldehyde and 0.2 % glutaraldehyde in 0.1 M PHEM for 2 hours at RT. Fixatives were removed by washing with 1 ml TDB and quenched with PBS + 0.15 % (w/v) glycine. Cells were pelleted and resuspended in 200 µl 12 % (w/v) gelatine (Rousselot 250 LP30) in 0.1 M PHEM at 37 °C and pelleted again. The pellets were solidified on ice, cut into smaller blocks, and infused with 2.3 M sucrose in 0.1 M PHEM overnight at 4 °C. The blocks were mounted on metal pins and stored in liquid nitrogen. The gelatine-embedded cells were cryosectioned to 55 nm or 250 nm thick sections at -120 °C or -100 °C, respectively, with a DiATOME diamond knife in a Leica ultracut cryomicrotome (UC7). Sections were collected and deposited on formvar- and carbon-coated grids using 2.3 M sucrose and 1.8 % (v/v) methylcellulose (MC; Sigma M6385 25 centipoises) mixed 1:1.

For Epon embedding, sample preparation and sectioning were performed as previously described (Langreth and Balber, 1975; Webster, 1989). In short, chemically fixed cells were pelleted (1500 x *g*, 10 min, RT) and washed 6 x in 0.12 M sucrose, 0.1 M cacodylate, pH 7.4. They were postfixed in 1 % (w/v) osmium tetroxide, stained *en bloc* in 1 % (w/v) uranyl acetate in 50 mM sodium maleate buffer (pH 5.1), dehydrated with ethanol and embedded at 60 °C in epoxy resin. Cells incubated with HRP were treated, in suspension, with diaminobenzidine (DAB) in 50 mM Tris-HCl (pH 7.6) containing 0.01 % (v/v) osmium tetroxide for 5 min prior to postfixation with 1 % osmium tetroxide. The epon-embedded cells were sectioned to 250 nm thick sections at RT.

Immuno-electron microscopy

Grids with sections facing down were incubated in a 24-well plate with 2 ml PBS at 37 °C for 30 – 60 min to remove gelatine, 2.3 M sucrose and 1.8 % MC mixture. Afterwards, the grids were washed on ~ 100 µl drops of PBS + 0.15 % (w/v) glycine and PBS on parafilm at RT (both 3 x 5 min). The standard volume for all non-antibody related steps was100 µl. Next, blocking was performed in PBS + 0.1 % (v/v) acetylated BSA (BSA-c, Aurion) + 0.5 % (w/v) cold fish-skin gelatine (FSG, Sigma) for 30 min. The following primary antibody incubation was done for 1 – 2 hours in PBS + 0.1 % BSA-c + 0.5 % FSG. The used antibody dilutions were rat anti-TbRab5A 1:50, guinea pig anti-TbRab7 1:50, rabbit anti-TbRab11 1:25, and rabbit anti-VSG 1:50. After that, grids were washed 5 x 5 min with PBS + 0.1 % BSA-c + 0.5 % FSG and incubated with corresponding gold coupled secondary antibodies for 1 – 2 hours (diluted 1:10 in PBS + 0.1 % BSA-c + 0.5 % FSG). Further washing steps with PBS + 0.1 % BSA-c + 0.5 % FSG (3 x 5 min) and PBS (3 x 5 min) followed before all remaining antibodies were fixed with 1.25 % glutaraldehyde for 5 min at RT. After three washing steps with ddH_2O to remove phosphate from the grids, sample contrast was increased by 5 min incubation on 2 % (w/v) uranyl acetate (UA) in water (pH 7) and 7 min incubation on 1.8 % (v/v) MC/ 0.3 % (w/v) UA in water (pH 4) (both on ice). Grids were retrieved with a metal ring and excess MC/UA was removed with filter paper. Grids were dried for at least 30 min at RT in the metal ring.

Electron Microscopes

JEOL JEM-2100 transmission electron microscope (TEM) operated at 200 kV with camera system: TVIPS F416 4k x 4k.

JEOL JEM-1400 Flash scanning transmission electron microscope (STEM) operated at 120 kV with camera system: Matataki Flash 2k x 2k.

FEI Tecnai TF30 transmission electron microscope (TEM) operated at 300kV with camera system: Gatan US4000 4k x 4k CCD.

The software Serial EM was used for tilt series acquisitions of electron tomograms. The subsequent reconstruction and segmentation were done using the IMOD software package (Kremer et al., 1996). For 2D electron micrographs pseudo colouring and highlighting was done using Adobe Illustrator 2022.

Immunoblotting

Trypanosomes were resuspended and lysed in protein sample buffer (60 mM Tris-HCl, pH 6.8, 2 % (w/v) SDS, 10 % (v/v) glycerol, 0.002 % (w/v) bromophenol blue, 1 % (v/v) β-mercaptoethanol) to yield equivalents of 2 x 10^5 cells/µl. For quantification of TbRab proteins by Western Blot 20 µl of the protein sample was resolved on 12.5 % SDS-PAGE gels and transferred onto nitrocellulose membrane. The membranes were blocked for 1 h at room temperature with 5 % (w/v) milk powder in PBS. Next, the membranes were incubated in polyclonal primary antibodies diluted in PBS containing 1 % (w/v) powdered milk and 0.1 % (v/v) Tween 20, anti-TbRab 1:5000 and monoclonal mouse anti-TbPFR (L13D6) 1:20 (Kohl et al., 1999). After wash steps, the membranes were incubated in IRDye 800 CW (Li-Cor) labelled either goat anti-rat, donkey anti-guinea pig, or donkey anti-rabbit and IRDye 680 LT (Li-Cor) labelled goat anti-mouse secondary antibodies diluted 1:10,000 in PBS containing 1 % (w/v) milk powder and 0.1 % (v/v) Tween 20. Images were acquired and quantified with the Li-Cor Odyssey system.

Recombinant protein expression and purification for antibody generation

The TbRab5A (Tb927.10.12960), TbRab7 (Tb927.9.11000), TbRab11 (Tb927.8.4330) open reading frames were amplified from *Trypanosoma brucei brucei* strain Lister 427 genomic DNA by PCR. The PCR product was digested with NdeI and XhoI restriction enzymes and ligated into the pET21-a expression vector, which encodes an N-terminal His6 tag. The plasmid was used to perform a chemical transformation into *E. coli* strain Rosetta II (DE3) pLysS. Individual colonies were subsequently grown at 37 °C in presence of 100 µg/ml ampicillin to an OD600 of ~ 0.8. Recombinant protein expression was induced by the addition of 50 µM IPTG and the cells were incubated for 4 h at 37 °C with shaking. Cells were harvested by centrifugation (3000 x *g*, 10 min, 4 °C). The pellet was resuspended in 10 ml lysis buffer (100 mM NaH_2PO_4, 10 mM Tris/ HCl, 8M Urea, pH 8.0) and incubated for 1 h at RT on. Final lysis was then achieved with sonication on ice, using 6 cycles for 10 s with MiniTip step 7 (Sonifier, B-12, Branson Ultrasonics). Lysates were clarified by centrifugation (10,000 x *g*, 30 min, RT) and incubated for 1 hour with Ni-NTA His bind resin (Merck) rolling at RT. Afterwards, the resin was transferred to a HiTrap column (GE healthcare) and washed with 30 ml lysis buffer and 30 ml buffer B (100 mM NaH_2PO_4, 10 mM Tris/ HCl, 8 M Urea, pH 6.3). Next, the bound proteins were eluted with 1 x 2 ml buffer C (100 mM NaH_2PO_4, 10 mM Tris/ HCl, 8 M Urea pH, 5.9), 1 x 2ml buffer D (100 mM NaH_2PO_4, 10 mM Tris/ HCl, 8M Urea pH 4.5) and 1 x 2 ml buffer E (100 mM NaH_2PO_4, 10 mM Tris/ HCl, 8 M Urea, pH 4.5 + 250 mM imidazole).

All elution's were then separately dialysed overnight against a 20 mM phosphate buffer (2.7 mM Na_2HPO_4, 17.3 mM NaH_2PO_4) at 4 °C. The purification success was validated by 15 % SDS-PAGE and proteins were sent to different companies for antibody generation.

Antibody generation

Recombinant full-size proteins were used to immunise different animals (Pineda, Berlin, Germany; Davids Biotechnology, Regensburg, Germany; Eurogentec, Seraing, Belgium). The resulting antisera were affinity purified against the immobilised recombinant protein. The resulting antisera from two rats (anti-TbRab5A) showed no need for affinity purification. All antibodies were validated for selectivity through immunoblots of the corresponding RNAi cell line (Supplementary 2).

HaloTag ligand labelling

HaloTag-Ligand-Amine (Promega, #P6741) was reconstituted in DMF (Sigma-Aldrich, #70547) to a concentration of 10 g/l. 250 µg HaloTag-Ligand Amine was conjugated to Alexa Fluor 647-NHS (Thermofisher, #A20006) by adding 150 µg of NHS-dye from a 10 g/l stock solution in DMF. The total reaction volume was adjusted to 120 µl with DMF, then DIPEA Base (Sigma-Aldrich, #387649) was added at 1:100. The reaction was incubated under gentle agitation and protected from light at room temperature for three hours. The reaction mixture was purified by reverse-phase high performance liquid chromatography (HPLC, Jasco) using a biphenyl column (Kinetex, #00F-4622-E0) with a solvent gradient of 0-60 % (v/v) acetonitrile (Sigma-Aldrich, #34851) in 0.1 % TFA (Sigma-Aldrich, #T6508) in water run over 30 min. Collected product fractions were dried in a speed-vac (Thermofisher, #SPD111V) and dissolved in DMSO.

Acknowledgements

We thank the Cell Microscopy Core of UMC Utrecht for their workshop "Cryosectioning and immuno-electron microscopy" and the opportunity to learn the Tokuyasu technique. Manfred Alsheimer provided protocols and advice with recombinant protein expression and antibody generation. Daniela Bunsen and Claudia Gehring-Höhn provided help with the EM benchwork and assistance with the electron microscope. Bernardo Gabiatti, Janna Eilts, Marcel Rühling and Tobias Kunz provided protocols and advice on expansion microscopy. We are grateful to Brooke Morriswood for essential discussions.

Funding

ME was supported by DFG grants EN305, SPP1726 (Microswimmers—From Single Particle Motion to Collective Behaviour), GIF grant I-473-416.13/2018 (Effect of extracellular *Trypanosoma brucei* vesicles on collective and social parasite motility and development in the tsetse fly) and GRK2157 (3D Tissue Models to Study Microbial Infections by Obligate Human Pathogens), the EU ITN Physics of Motility, and the BMBF NUM Organo-Strat. ME is a member of the Wilhelm Conrad Röntgen Center for Complex Material Systems (RCCM). The transmission electron microscopes in Würzburg were funded by the Deutsche Forschungsgemeinschaft (DFG, German Research Foundation) – 426173797 (INST 93/1003-1 FUGG) and 218894163. AB was supported by the Brazilian agency CAPES (program: CAPES/DAAD—Call No. 22/2018; process 88881.199683/2018-01). MJ was supported by GRK2157 and the European Research Council (ERC) under the European Union's Horizon 2020 research and innovation programme (grant agreement No 835102) awarded to MS.

References

Alcantara, C.L., de Souza, W., and da Cunha, E.S.N.L. (2018). Tridimensional Electron Microscopy Analysis of the Early Endosomes and Endocytic Traffic in *Trypanosoma cruzi* Epimastigotes. Protist *169*, 887-910.

Allen, C.L., Goulding, D., and Field, M.C. (2003). Clathrin-mediated endocytosis is essential in *Trypanosoma brucei*. EMBO J *22*, 4991-5002.

Alonso, V.L. (2022). Ultrastructure Expansion Microscopy (U-ExM) in *Trypanosoma cruzi*: localization of tubulin isoforms and isotypes. Parasitology Research *121*, 3019-3024.

Alsford, S., Kawahara, T., Glover, L., and Horn, D. (2005). Tagging a *T. brucei* RRNA locus improves stable transfection efficiency and circumvents inducible expression position effects. Mol Biochem Parasitol *144*, 142-148.

Amodeo, S., Kalichava, A., Fradera-Sola, A., Bertiaux-Lequoy, E., Guichard, P., Butter, F., and Ochsenreiter, T. (2021). Characterization of the novel mitochondrial genome segregation factor TAP110 in *Trypanosoma brucei*. Journal of Cell Science *134*, jcs254300.

Ansari, I., Basak, R., and Mukhopadhyay, A. (2022). Hemoglobin Endocytosis and Intracellular Trafficking: A Novel Way of Heme Acquisition by *Leishmania*. Pathogens *11*.

Bartossek, T., Jones, N.G., Schafer, C., Cvitkovic, M., Glogger, M., Mott, H.R., Kuper, J., Brennich, M., Carrington, M., Smith, A.S.*, et al.* (2017). Structural basis for the shielding function of the dynamic trypanosome variant surface glycoprotein coat. Nat Microbiol *2*, 1523-1532.

Becker, M., Aitcheson, N., Byles, E., Wickstead, B., Louis, E., and Rudenko, G. (2004). Isolation of the repertoire of VSG expression site containing telomeres of *Trypanosoma brucei* 427 using transformation-associated recombination in yeast. Genome Res *14*, 2319-2329.

Benchimol, M., and de Souza, W. (2022). *Giardia intestinalis* and its endomembrane system. Journal of Eukaryotic Microbiology *69*, e12893.

Borges, A.R., Link, F., Engstler, M., and Jones, N.G. (2021). The Glycosylphosphatidylinositol Anchor: A Linchpin for Cell Surface Versatility of Trypanosomatids. Frontiers in Cell and Developmental Biology *9*.

Burki, F., Roger, A.J., Brown, M.W., and Simpson, A.G.B. (2020). The New Tree of Eukaryotes. Trends in Ecology & Evolution *35*, 43-55.

Chaves, I., Rudenko, G., Dirks-Mulder, A., Cross, M., and Borst, P. (1999). Control of variant surface glycoprotein gene-expression sites in *Trypanosoma brucei*. EMBO J *18*, 4846-4855.

Chen, F., Tillberg, P.W., and Boyden, E.S. (2015). Optical imaging. Expansion microscopy. Science *347*, 543-548.

Chi, R.J., Harrison, M.S., and Burd, C.G. (2015). Biogenesis of endosome-derived transport carriers. Cell Mol Life Sci *72*, 3441-3455.

Costes, S.V., Daelemans, D., Cho, E.H., Dobbin, Z., Pavlakis, G., and Lockett, S. (2004). Automatic and quantitative measurement of protein-protein colocalization in live cells. Biophys J *86*, 3993-4003.

Cross, G.A. (1975). Identification, purification and properties of clone-specific glycoprotein antigens constituting the surface coat of *Trypanosoma brucei*. Parasitology *71*, 393-417.

Engstler, M., and Boshart, M. (2004). Cold shock and regulation of surface protein trafficking convey sensitization to inducers of stage differentiation in *Trypanosoma brucei*. Genes Dev *18*, 2798-2811.

Engstler, M., Pfohl, T., Herminghaus, S., Boshart, M., Wiegertjes, G., Heddergott, N., and Overath, P. (2007). Hydrodynamic flow-mediated protein sorting on the cell surface of trypanosomes. Cell *131*, 505-515.

Engstler, M., Thilo, L., Weise, F., Grunfelder, C.G., Schwarz, H., Boshart, M., and Overath, P. (2004). Kinetics of endocytosis and recycling of the GPI-anchored variant surface glycoprotein in *Trypanosoma brucei*. J Cell Sci *117*, 1105-1115.

Gambarotto, D., Zwettler, F.U., Le Guennec, M., Schmidt-Cernohorska, M., Fortun, D., Borgers, S., Heine, J., Schloetel, J.-G., Reuss, M., and Unser, M. (2019). Imaging cellular ultrastructures using expansion microscopy (U-ExM). Nature Methods *16*, 71-74.

1232 Gorilak, P., Pružincová, M., Vachova, H., Olšinová, M., Schmidt Cernohorska, M., and Varga, V. (2021).
1233 Expansion microscopy facilitates quantitative super-resolution studies of cytoskeletal structures in
1234 kinetoplastid parasites. Open Biology *11*, 210131.
1235 Grünfelder, C.G., Engstler, M., Weise, F., Schwarz, H., Stierhof, Y.D., Boshart, M., and Overath, P.
1236 (2002). Accumulation of a GPI-anchored protein at the cell surface requires sorting at multiple
1237 intracellular levels. Traffic *3*, 547-559.
1238 Grünfelder, C.G., Engstler, M., Weise, F., Schwarz, H., Stierhof, Y.D., Morgan, G.W., Field, M.C., and
1239 Overath, P. (2003). Endocytosis of a glycosylphosphatidylinositol-anchored protein via clathrin-coated
1240 vesicles, sorting by default in endosomes, and exocytosis via RAB11-positive carriers. Mol Biol Cell *14*,
1241 2029-2040.
1242 Gull, K. (2003). Host–parasite interactions and trypanosome morphogenesis: a flagellar pocketful of
1243 goodies. Current Opinion in Microbiology *6*, 365-370.
1244 Hartel, A.J., Glogger, M., Jones, N.G., Abuillan, W., Batram, C., Hermann, A., Fenz, S.F., Tanaka, M., and
1245 Engstler, M. (2016). N-glycosylation enables high lateral mobility of GPI-anchored proteins at a
1246 molecular crowding threshold. Nat Commun *7*, 12870.
1247 Heilemann, M., van de Linde, S., Schuttpelz, M., Kasper, R., Seefeldt, B., Mukherjee, A., Tinnefeld, P.,
1248 and Sauer, M. (2008). Subdiffraction-resolution fluorescence imaging with conventional fluorescent
1249 probes. Angew Chem Int Ed Engl *47*, 6172-6176.
1250 Hirumi, H., and Hirumi, K. (1989). Continuous cultivation of *Trypanosoma brucei* blood stream forms
1251 in a medium containing a low concentration of serum protein without feeder cell layers. J Parasitol *75*,
1252 985-989.
1253 Jones, N.G., Thomas, E.B., Brown, E., Dickens, N.J., Hammarton, T.C., and Mottram, J.C. (2014).
1254 Regulators of *Trypanosoma brucei* cell cycle progression and differentiation identified using a kinome-
1255 wide RNAi screen. PLoS Pathog *10*, e1003886.
1256 Kalichava, A., and Ochsenreiter, T. (2021). Ultrastructure expansion microscopy in *Trypanosoma*
1257 *brucei*. Open Biology *11*, 210132.
1258 Link, F., Borges, A.R., Jones, N.G., and Engstler, M. (2021). To the Surface and Back: Exo- and Endocytic
1259 Pathways in *Trypanosoma brucei*. Front Cell Dev Biol *9*, 720521.
1260 Mayor, S., Presley, J.F., and Maxfield, F.R. (1993). Sorting of membrane components from endosomes
1261 and subsequent recycling to the cell surface occurs by a bulk flow process. Journal of Cell Biology *121*,
1262 1257-1269.
1263 McGovern, O.L., Rivera-Cuevas, Y., and Carruthers, V.B. (2021). Emerging Mechanisms of Endocytosis
1264 in *Toxoplasma gondii*. Life *11*, 84.
1265 Mironov, A.A., Beznoussenko, G.V., Trucco, A., Lupetti, P., Smith, J.D., Geerts, W.J., Koster, A.J., Burger,
1266 K.N., Martone, M.E., and Deerinck, T.J. (2003). ER-to-Golgi carriers arise through direct en bloc
1267 protrusion and multistage maturation of specialized ER exit domains. Developmental Cell *5*, 583-594.
1268 Möbius, W., and Posthuma, G. (2019). Sugar and ice: Immunoelectron microscopy using cryosections
1269 according to the Tokuyasu method. Tissue Cell *57*, 90-102.
1270 Mogelsvang, S., Gomez-Ospina, N., Soderholm, J., Glick, B.S., and Staehelin, L.A. (2003). Tomographic
1271 Evidence for Continuous Turnover of Golgi Cisternae in *Pichia pastoris*. Molecular Biology of the Cell
1272 *14*, 2277-2291.
1273 Morgan, G.W., Allen, C.L., Jeffries, T.R., Hollinshead, M., and Field, M.C. (2001). Developmental and
1274 morphological regulation of clathrin-mediated endocytosis in *Trypanosoma brucei*. J Cell Sci *114*, 2605-
1275 2615.
1276 Mugnier, M.R., Stebbins, C.E., and Papavasiliou, F.N. (2016). Masters of Disguise: Antigenic Variation
1277 and the VSG Coat in *Trypanosoma brucei*. PLoS Pathog *12*, e1005784.
1278 Overath, P., and Engstler, M. (2004). Endocytosis, membrane recycling and sorting of GPI-anchored
1279 proteins: *Trypanosoma brucei* as a model system. Mol Microbiol *53*, 735-744.
1280 Overath, P., Stierhof, Y.D., and Wiese, M. (1997). Endocytosis and secretion in trypanosomatid
1281 parasites - Tumultuous traffic in a pocket. Trends Cell Biol *7*, 27-33.
1282 Podinovskaia, M., Prescianotto-Baschong, C., Buser, D.P., and Spang, A. (2021). A novel live-cell
1283 imaging assay reveals regulation of endosome maturation. Elife *10*.

Podinovskaia, M., and Spang, A. (2018). The Endosomal Network: Mediators and Regulators of Endosome Maturation. In Endocytosis and Signaling, C. Lamaze, and I. Prior, eds. (Cham: Springer International Publishing), pp. 1-38.

Porto-Carreiro, I., Attias, M., Miranda, K., De Souza, W., and Cunha-e-Silva, N. (2000). *Trypanosoma cruzi* epimastigote endocytic pathway: cargo enters the cytostome and passes through an early endosomal network before storage in reservosomes. Eur J Cell Biol *79*, 858-869.

Poteryaev, D., Datta, S., Ackema, K., Zerial, M., and Spang, A. (2010). Identification of the switch in early-to-late endosome transition. Cell *141*, 497-508.

Redmond, S., Vadivelu, J., and Field, M.C. (2003). RNAit: an automated web-based tool for the selection of RNAi targets in *Trypanosoma brucei*. Mol Biochem Parasitol *128*, 115-118.

Rink, J., Ghigo, E., Kalaidzidis, Y., and Zerial, M. (2005). Rab conversion as a mechanism of progression from early to late endosomes. Cell *122*, 735-749.

Rose, C., Casas-Sánchez, A., Dyer, N.A., Solórzano, C., Beckett, A.J., Middlehurst, B., Marcello, M., Haines, L.R., Lisack, J., Engstler, M.*, et al.* (2020). *Trypanosoma brucei* colonizes the tsetse gut via an immature peritrophic matrix in the proventriculus. Nature Microbiology *5*, 909-916.

Schwebs, M., Paul, T., Glogger, M., Forster, L., Morriswood, B., Teßmar, J., Groll, J., Engstler, M., Kollmannsberger, P., and Fenz, S. (2022). Single-molecule fluorescence microscopy demonstrates fast dynamics of the variant surface glycoprotein coat on living trypanosomes. bioRxiv, 2022.2008.2003.502583.

Slot, J.W., and Geuze, H.J. (2007). Cryosectioning and immunolabeling. Nat Protoc *2*, 2480-2491.

Stoorvogel, W., Strous, G.J., Geuze, H.J., Oorschot, V., and Schwartz, A.L. (1991). Late endosomes derive from early endosomes by maturation. Cell *65*, 417-427.

Strassert, J.F.H., Irisarri, I., Williams, T.A., and Burki, F. (2021). A molecular timescale for eukaryote evolution with implications for the origin of red algal-derived plastids. Nat Commun *12*, 1879.

Taylor, J.E., and Rudenko, G. (2006). Switching trypanosome coats: what's in the wardrobe? Trends in Genetics *22*, 614-620.

Tillberg, P.W., Chen, F., Piatkevich, K.D., Zhao, Y., Yu, C.C., English, B.P., Gao, L., Martorell, A., Suk, H.J., Yoshida, F.*, et al.* (2016). Protein-retention expansion microscopy of cells and tissues labeled using standard fluorescent proteins and antibodies. Nat Biotechnol *34*, 987-992.

van der Beek, J., de Heus, C., Liv, N., and Klumperman, J. (2021). Quantitative correlative microscopy reveals the ultrastructural distribution of endogenous endosomal proteins. Journal of Cell Biology *221*.

Vines, J.H., and King, J.S. (2019). The endocytic pathways of *Dictyostelium discoideum*. Int J Dev Biol *63*, 461-471.

Wirtz, E., Leal, S., Ochatt, C., and Cross, G.A. (1999). A tightly regulated inducible expression system for conditional gene knock-outs and dominant-negative genetics in *Trypanosoma brucei*. Mol Biochem Parasitol *99*, 89-101.